A RANS ANALYSIS OF PRESSURIZED THERMAL SHOCK PHENOMENA IN NUCLEAR REACTOR GEOMETRIES USING STARCCM+.

A Thesis

by

JOHN P. MULLOY JR

Submitted to the Office of Graduate and Professional Studies of
Texas A&M University
in partial fulfillment of the requirements for the degree of

MASTER OF SCIENCE

Chair of Committee,	Yassin Hassan
Committee Members,	Maria King
	Rodolfo Vaghetto
Head of Department,	Yassin Hassan

August 2018

Major Subject: Nuclear Engineering

ABSTRACT

Computational fluid dynamics (CFD) simulations were conducted using Star CCM+ in order to investigate the mixing characteristics in the cold leg injection region of a pressurized water reactor (PWR) pressure vessel. Through the use of CFD codes, this present work seeks to characterize the mixing in this region in order to provide information capable of impacting the reactor lifetime. The flow in the domain is driven solely by buoyancy, through the use of two varying density fluids in an isothermal setup. The fluids used in the experiment were a salt-water and ethanol-water mixture, for both the heavy fluid and light fluid respectively. The simulated density difference was chosen to be 10% and the cold tank fluid height was adjusted such that the static pressure across the initial fluid-fluid interface would be zero. The simulation was conducted in the Reynolds Averaged Navier-Stokes (RANS) framework, with focus on K-epsilon model. Turbulent parameters and values for densities, velocities and Reynolds stresses were gathered at locations of interest. These quantities of interest were gathered with the intent on guiding the experimental analysis in preparation for a future verification and validation study for the committee on the safety of nuclear installations. The simulated results deviate from the available experimental data, this is due to a change in the material properties and the solutions used in the experimental analysis. Despite this, the simulations of the cold-leg mixing experiment behave physically as expected.

DEDICATION

For my Mother, Chasity Y. Mulloy, my Father, John P Mulloy

and my brothers and sisters.

ACKNOWLEDGMENTS

I would like to acknowledge the work conducted by the experimental group out at USB. The individuals whose hard work provided insight into my own are as follows:

1. Dr Rodolfo Vaghetto
2. Daniel Orea
3. Vasileios Kyriakopoulos
4. Jonah Haefner
5. Macon Heath
6. Blake Maher

CONTRIBUTORS AND FUNDING SOURCES

Contributors

The construction of the experimental facility and the collection of its data was done under the supervision of Dr. Rodolfo Vaghetto.

The experimental data utilized in this report was collected and post-processed by Daniel Orea and Vasileios Kyriakopoulos.

Funding Sources

Graduate school was funded, in part, by the pathways to the doctorate fellowship from the TAMU OGAPS

NOMENCLATURE

OGAPS	Office of Graduate and Professional Studies at Texas A&M University
TAMU	Texas A&M University
CFD	Computational Fluid Dynamics
CSNI	Committee on the Safety of Nuclear Installations
NRC	Texas A&M University
TAMU	Texas A&M University
RANS	Reynolds Averaged Navier-Stokes
LES	Large Eddy Simulation
DNS	Direct Numerical Simulation
CAD	Computer Aided Design
EIA	Energy Information Administration
ECCS	Emergency Core Cooling System
HPCI	High Pressure Coolant Injection
LOCA	Loss Of Coolant Accident
RHR	Residual Heat Removal
ROCOM	Rossendorf Coolant Mixing Model
V&V	Verification and Validation
RST	Reynolds Stress Turbulence
CLM	Cold-Leg Mixing
NEA	Nuclear Energy Agency

KEM	K-ϵ Model
TLF	Two-Layer Formulation
GCI	Grid Convergence Index

TABLE OF CONTENTS

Page

LIST OF FIGURES

FIGURE Page

LIST OF TABLES

TABLE Page

1. INTRODUCTION AND LITERATURE REVIEW

The world demand for electricity has steadily grown over the last several decades and it is projected, by the Energy Information Administration (EIA), to continue to grow over the next 25 years. With the projected growth in energy demand estimated to be approximately 28% [1], the majority of which coming from non-OECD countries such as China and India, it is critical that safe, affordable and efficient energy sources be employed. While the research efforts directed towards renewable energy resources are certainly laudable, there are no alternatives staged to supplant the base load capability that nuclear power provides.

Nuclear accidents, such as the ones that occurred at Chernobyl in 1986, Three Mile Island in 1979 and Fukushima in 2011, don't do much to help public perception of the safety and viability of nuclear power. In order to maintain and further develop the trust of the public, in regards to nuclear power technology, engineers must design and develop new active and passive safety systems. It is not enough however to simply demand the development of better safety systems. In order to develop these safety systems an understanding of the physics underlying the accident causing conditions must be obtained. In this study the physics of buoyancy, scalar stratification and turbulent mixing are of primary importance.

One safety system component of the Emergency Core Cooling System (ECCS), is the High Pressure Coolant Injection System (HPCI) which is designed to account for a multitude of accident conditions, e.g. Loss of Cool Accident (LOCA). The concept of the HPCI system is simple, when the core is overheating or when a LOCA is occurring, pumps activate and begin injecting high pressure coolant in an effort to cool down the reactor core. However, as with most complex systems, the introduction of one variable often leads to a

slue of new considerations that must be taken into account. The effects of rapidly injecting cooler fluid in to the core are not confined to the thermal field alone. Mechanically the injection of cold fluid near the core can cause rapid changes to the internal stresses in the reactor vessel. Additionally the cold fluid, as it begins to heat up, can begin to expand thus increasing the system pressure and further adding to the stresses that both the reactor and pressure vessels are subjected to.

Of the nuclear accidents listed the one which is most relevant to this work is the Fukushima Daiichi accident. This accident was the result of a devastating 9.0 earthquake off of the coast of Japan. Reactor units 1, 2 & 3, which were operating at the time of the quake, were automatically shut down as per procedure. This shut down meant that the Residual Heat Removal (RHR) systems couldn't rely on locally generated power and thus needed to draw their power from auxiliary systems such as on-site emergency diesel generators. What wasn't anticipated was the severity of the resulting tsunami which, to the misfortune of those managing the plant, took the emergency diesel generators offline. With the diesel generators offline and the batteries only capable of providing short term power to the RHR systems, the reactors began proceeding towards an unstable state. The rapid increase in temperature in the reactor resulted in an increased rate of oxidization reactions between the metals found in the reactor and the reactor coolant, a byproduct of these reactions being hydrogen gas. Once enough hydrogen gas pooled at the top of the reactor containment facility it was only a matter of time before said gas detonated. The application of the work contained within this study can be applied to a litany of problems related to the Daiichi accident. In his thesis [2] Fatih Sarikurt conducted a Verification and Validation study focusing on the stratification of hydrogen gas within a reactor containment building. While similar in nature this study will not focus on hydrogen stratification within the containment vessel. Rather it will focus on cold leg buoyant mixing in the region between the pressure vessel wall and reactor core.

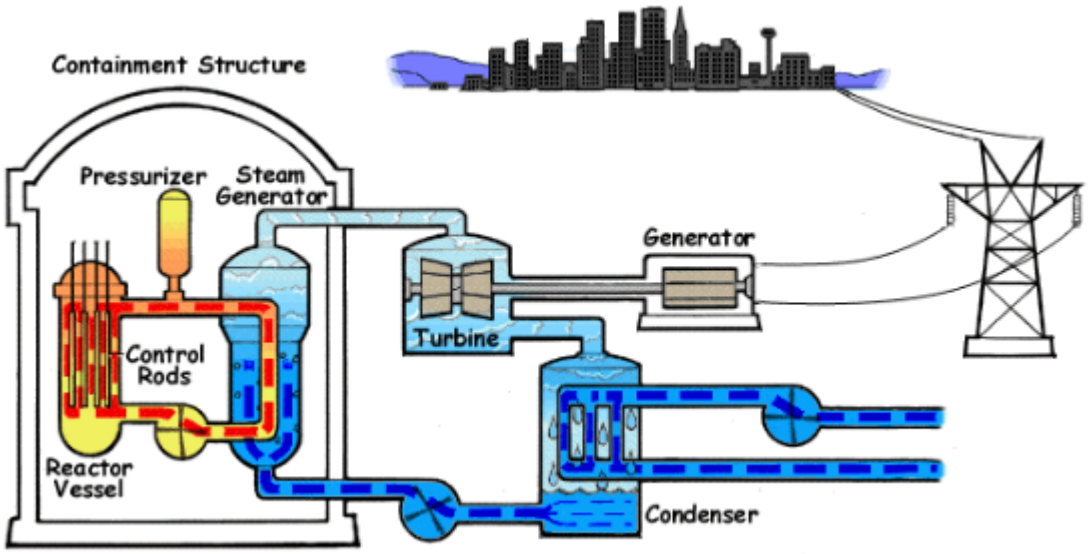

Figure 1.1: A schematic of a typical Pressurized Water Reactor (PWR) with the ECCS-HPCI loop included. Reprinted from [3]

As previously mentioned the HPCI, an ECC subsystem, plays an integral part in the active cooling of a nuclear reactor. A crude diagram of a PWR is shown in Figure 1.1. The bulk storage tank containing the cold fluid, the pipe which transports said fluid to the pressure vessel. i.e. the cold water feed-line or cold-leg, and reactor vessel are what comprise the domain of interest. Being able to characterize how buoyancy impacts the distribution of scalar quantities within the domain can enable the design of modern, safer and more efficient ECCS. The isolation of the buoyancy effects on the domain of interest is paramount to characterization of the turbulent mixing in the downcommer region of the reactor. Given that the temperature differences within a typical pressurized water reactor are approximately 30-37 degrees Celsius, equivalent to a 10-12% difference between the mixing hot and cold fluids, density should contributions to the flow should not be trivialized.

Buoyancy driven exist naturally in many forms and are an important factor in a vari-

ety of engineering applications. These buoyancy driven flows, often reffered to as gravity currents, have been studied extensively both experimentally and numerically [4, 5, 6]. In nuclear engineering buoyancy driven flows have been observed in LOCA in PWRs, making them a topic of relevance when discussing RHR and ECCS [7]. The characterization of this phenomena and its impact on cold leg mixing is critical to reactor pressure vessel (RPV) integrity assessment calculations, be they for the design of new reactor concepts or the lifetime extensions of the current fleet.

Many investigations have sought to characterize the effects of buoyancy on scalar quantity distribution within a reactor-like computational domain. The Rossendorf Coolant Mixing Model (ROCOM) benchmark reproduces, geometrically, the German KONVOI-type reactor [8] in an attempt to characterize the passive scalar distribution in the downcommer during forced convection scenarios. A slection of papers which participated in a V&V study of this domain are presented here due to their similarity to the domain of interest in this work. The work conducted by Toppila [9] focused on simulating the ROCOM geometry using ANSYS Fluent with the intent on evaluating the scalar distribution in the downcommer region. They claim to have found a mild agreement between their time averaged, 200-648 seconds, concentration data and the experimental results. It should be noted, however, they make no comparisons with velocity data as it was not collected in the ROCOM experiment. Another study conducted by Hohne et al. [10] used the Reynolds Stress Turbulence (RST) model in CFX-5 and Large Eddy Simulation in a code called Trio_U to simulate the flow. The RST model was reported to exhibited a transient lag and bot simulation methodologies were reported to have a good qualitative agreement with the experimental data provided.

While similar in methodology and objective the ROCOM benchmark studies vastly differ from those conducted within this work. In Figures 1.2 & 1.3. are pictures of a typical PWR reactor vessel, and the Texas A&M University (TAMU) Cold-Leg Mixing

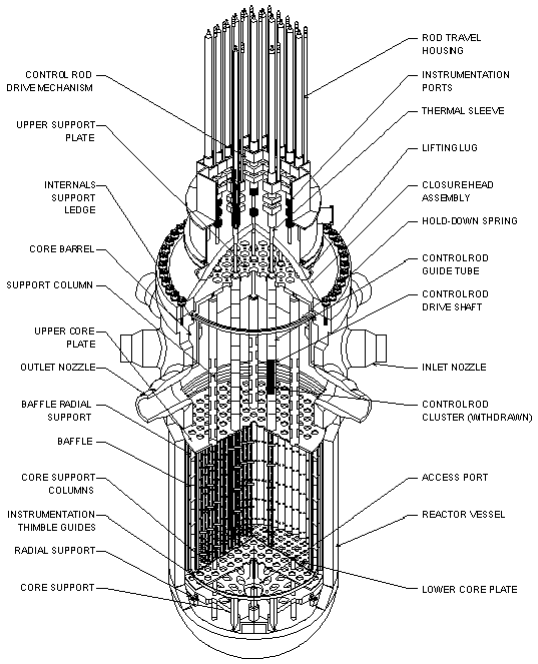

Figure 1.2: A detailed schematic of a typical PWR reactor vessel. Reprinted from [11]

(CLM) experimental geometry respectively. One difference, that can be seen between the two figures, is that the typical vessel is comprised of multiple legs hot & cold whereas the TAMU CLM experiment consists of two tanks and one leg. A comparison provided in Figures 1.2 & 1.3 shows the difference between a typical PWR reactor vessel and the vessel in the TAMU-CLM experiment. While the typical PWR vessel could be simulated as an open system, which lends itself to temporal averaging, the TAMU-CLM facility is a closed system of finite energy and has no inlets or outlets thus making the representation of data all that more difficult. The last, and probably the most important, distinction between the operation of the two facilities is that the typical PWR simulations focus on forced convection whereas the TAMU-CLM facility is a natural convection facility.

The objective of this work, much like the objectives of the surveyed literature, is the comparison of the simulated results with those generated by the preliminary experimental

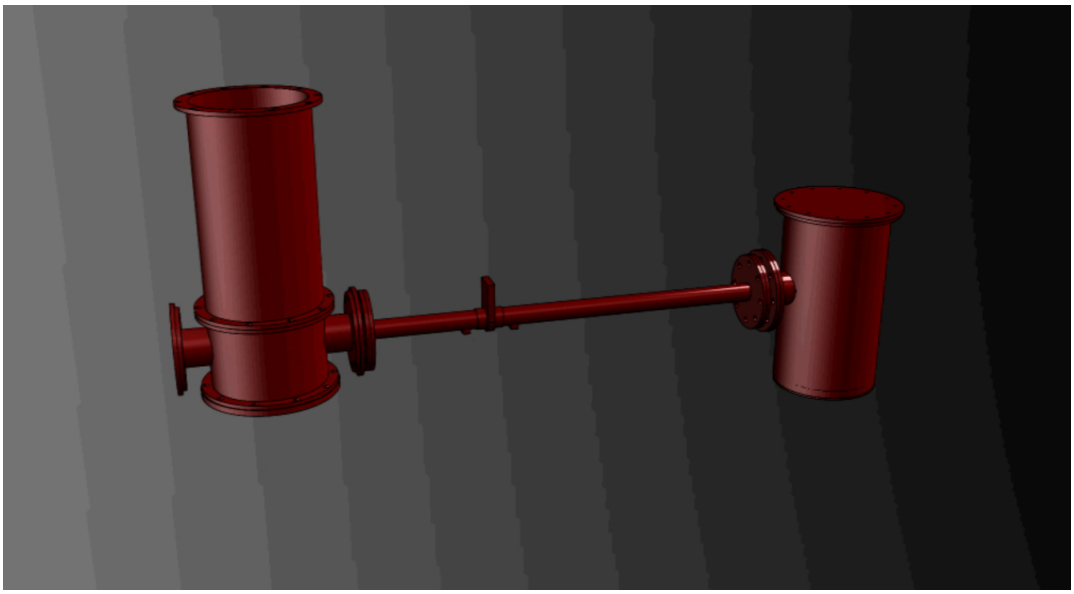

Figure 1.3: A Solidworks representation of the TAMU CLM benchmark

data. This is in preparation for the 5^{th} V&V benchmark, organized by the Nuclear Energy Agency (NEA) Committee on the Safety of Nuclear Installations (CSNI), which will focus on nuclear safety issues with cold leg mixing in the presence of buoyancy effects. Simulating buoyancy-driven flows brings about its own series of challenges. Namely dealing with the non-stationary nature of natural convection flows.

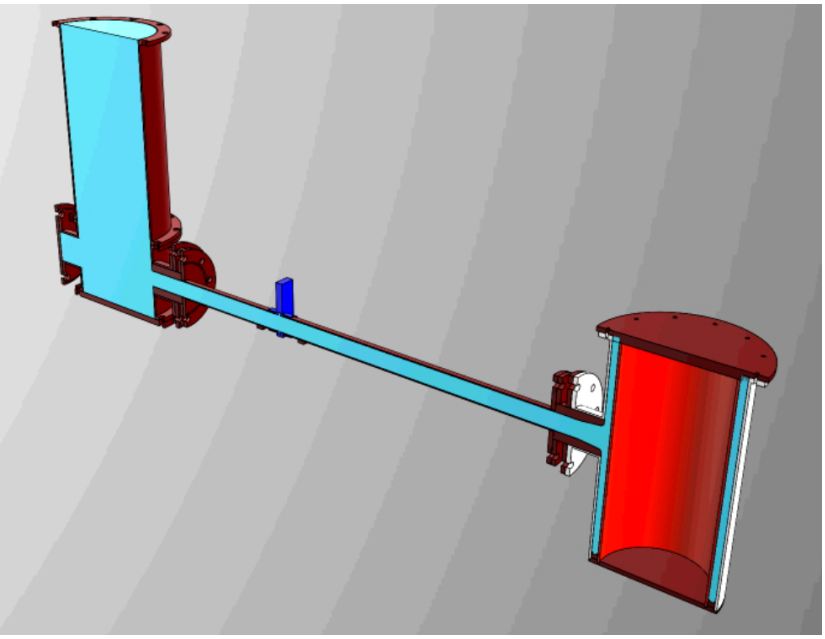

Figure 1.4: A Solidworks representation of the TAMU CLM benchmark, light blue is the fluid domain, maroon is the exterior wall, red is the reactor core wall and dark blue is the knife valve enclosure

The novelty of the presented simulation stems from the prototypical geometry, see Figure 1.4, and the fact that the flow is motivated through buoyant forces alone. Unlike previous NEA benchmarks wich featured open systems, such as PANDA and GEMIX [2, 12], the current simulations are of a closed, finite energy domain. Simulated geometries have ranged from simplified t-junctions [13, 14] to more representative reactor-like geometries [15]. While each study may have a particular topic or goal in mind when conducting their respective simulations. The overarching commonality is the characterization of cold-leg mixing in a downcommer-like region.

2. THEORY AND MATHEMATICS OF CFD AND TURBULENCE MODELING

2.1 History of CFD

Computational Fluid Dynamics (CFD), as its name implies, is a term used to generalize the study of fluids computationally. CFD has its roots in computer science, numerical analysis, statistics and various fields of engineering. Its utilization as a tool can be done in a near limitless number of fields. Before going through the rigor of the developing of a CFD code or selecting numerical procedures, one should first understand the physical phenomena which they are trying to simulate. Listed below are a couple of flow characteristics that will greatly vary the approach taken by any engineer attempting to utilize CFD tools.

1. Is the flow compressible or incompressible?
2. Is the flow Turbulent or Laminar?
3. Is the simulated flow multi-phase or single-phase?
4. What spatial and temporal resolution is required for the problem?
5. Are passive scalar quantities being transported?
6. Are scalar quantities actively changing the material properties?

Needless to say, the application of CFD tools is an incredibly flow specific task. Scientists have spend their lives focusing on smaller sub-sections of the enumerated list above. It is for this reason that the primary task of an engineer looking to use CFD should be to understand, to the greatest extent possible, the problem at hand.

Prior to the early 70's the concept of Computationally Aided Design (CAD) was in its infancy. Due to the cost of computers and their limited capability only the largest of engineering organizations could afford them. With breakthroughs in their capability and a reductions in cost these early computers rapidly proliferated to smaller firms and organizations. However, advances were not only made in the field of computational science. The overall understanding of turbulence and the ways in which it could be modeled were also seeing improvements at this time. The development of new turbulence models was necessitated by the limited computational resources available to scientists at the time. While both the availability and capability of computational resources have improved by orders of magnitude, the study and development of turbulence modeling hasn't slowed down.

2.2 Relevant Governing Equations

Regardless of the flow regime being analyzed the first step is to identify the relevant governing equations. For incompressible fluid flows, with no involvement of scalar quantities, the conservation of momentum can be expressed using the Navier-Stokes Equations, shown below in Eq. 2.1.

$$\rho\frac{\partial u_i}{\partial t} + \rho u_j\frac{\partial u_i}{\partial x_j} = -\rho\frac{\partial p}{\partial x_i} + \mu\frac{\partial^2 u_j}{\partial x_k x_k} + \rho g \tag{2.1}$$

Which is followed by the mass conservation equation, shown below in Eq. 2.2.

$$\nabla \bullet u = 0 \tag{2.2}$$

This equation consists of four major parts, depending on the flow being analyzed the body forces may become a fifth contributor. While body forces are present in this study, for mathematical simplicity they will be disregarded for now. Below, each remaining component of the Navier-Stokes equation is listed and discussed in the Eulerian framework.

- Unsteady Term

  $\rho\frac{\partial u_i}{\partial t}$, represents the temporal contribution to the fluid acceleration.

- Non-linear or Convective Term

  $\rho u_j\frac{\partial u_i}{\partial x_j}$, represents the convective contribution to the overall acceleration of the fluid i.e the spatial contribution towards acceleration.

- Pressure Term

  Pressure, $-\rho\frac{\partial p}{\partial x_j}$, its role is to ensure that the fluid field satisfies the continuity equation. It does this through the redistribution of energy to the various velocity components. The inner workings of this process have been the subject of intense study and will not be discussed in this thesis.

- Viscous Term

  $\mu\frac{\partial^2 u_j}{\partial x_k x_k}$, is the sink in the Navier-Stokes equation. It dampens the flow and ultimately transforms energy from momentum into internal energy.

2.2.1 Alternative Descriptions of the NS Equations

The previous description of incompressible fluid flow is easy and intuitive to derive from first principles i.e Newton's laws. It is not, however, particularly helpful is describing the multi-scaled nature of turbulence and how each term acts on said scales. In order to better understand the impact that varying scales of motion have on each of these terms a spectral description of the flow will be needed. While these mathematical descriptions of the flow are not required explicitly for this project their derivations prove to be a useful exercise in solidifying ones understanding of the governing equations and their impact on turbulent processes. The first step, done out of convenience, would be to non-dimensionalize Eq. 2.1. & Eq. 2.2. using Eq. 2.3-2.7.

$$x = x^{\star} L \tag{2.3}$$

$$t = t^{\star} \frac{U_0}{L} \tag{2.4}$$

$$\rho \frac{U_0^2}{L} \tag{2.5}$$

$$g = g^{\star} \overrightarrow{k} \tag{2.6}$$

$$u = u^{\star} U_0 \tag{2.7}$$

Once the above non-dimenalizations have been applied to Eq. 2.1. & Eq. 2.2 and each term has been divided by the term in Eq. 2.8

$$\rho \frac{U_0^2}{L} \tag{2.8}$$

you get Eq. 2.9. & Eq. 2.10.

$$\frac{\partial u_i^{\star}}{\partial t^{\star}} + u_j^{\star} \frac{\partial u_i^{\star}}{\partial x_j^{\star}} = -\frac{\partial p^{\star}}{\partial x_j^{\star}} + \frac{\mu}{\rho L U_0} \frac{\partial^2 u_j^{\star}}{\partial x_k^{\star} x_k^{\star}} + \frac{g^{\star} L}{U_0^2} \overrightarrow{k} \tag{2.9}$$

$$\nabla^{\star} \bullet u^{\star} = 0 \tag{2.10}$$

Recalling the definitions of the Reynolds number and the Froude number, shown below, one can further simplify the Eq. 6, to what is seen below in Eq. 8. This is the non-dimensionalized Navier-Stokes Equation

$$Re = \frac{\rho L U}{\mu} \tag{2.11}$$

$$Fr = \frac{gL}{U^2} \tag{2.12}$$

$$\frac{\partial u_i^\star}{\partial t^\star} + u_j^\star \frac{\partial u_i^\star}{\partial x_j^\star} = -\frac{\partial p^\star}{\partial x_j^\star} + \frac{1}{Re}\frac{\partial^2 u_j^\star}{\partial x_k^\star x_k^\star} + \frac{1}{Fr}\overrightarrow{k} \tag{2.13}$$

This form of the NS equations is incredibly useful in scaling analyses for both experimental and computational investigations. With that being said it still doesn't offer an intuitive description of the broadband nature that turbulence truly is. To get a better understanding of the NS equations, and how each term contributes towards a turbulent flow regime, a spectral decomposition of the non-dimensionalized NS equations will be applied on a term by term basis.

For simplification purposes, and to help keep this thesis a reasonable size, a mathematical discussion of the pressure's influence on turbulent processes will be neglected. Suffice it to say the roll of pressure in turbulence is to help maintain continuity within the flow. Having delegated the rigorous mathematical derivation of the pressure contribution to another paper what we are left with is the viscous Burgers equations. In order to derive the spectral form of Eq. 5. one must understand a couple of rules regarding the properties of averaging and Fourier transforms. Shown below in Eq. 2.14. & Eq. 2.15. are the formulations that allow one to convert a velocity signal described in physical space into a amplitude signal described in wave space. It should be noted that the angular brackets in Eq. 10. indicate a volume averaging operation.

$$u(x) = \sum_{k}^{\infty} \hat{u}(k) e^{ikx} \tag{2.14}$$

$$\hat{u}(k) =< u(x)e^{-ikx} >_L \tag{2.15}$$

With these two definitions, we can begin transforming each term of Eq. 8. Starting with the temporal operator and an understanding that Eq. 9 & Eq. 10 are not dependent on time, we can construct the spectral representation of the temporal term.

$$\frac{\partial \hat{u}(k)}{\partial t} = \frac{\partial u(x)}{\partial t} \tag{2.16}$$

Moving on to the viscous term in Eq. 8. and understanding that each spatial derivative of Eq. 9 & Eq. 10 yields an ik term we can construct the following relationship.

$$\frac{1}{Re}\frac{\partial^2 u_j}{\partial x_k x_k} = \frac{i^2 k^2}{Re}\hat{u}(k) = \frac{-k^2}{Re}\hat{u}(k) \tag{2.17}$$

Now it should be noted that because we are looking to create the spectral representation of the viscous Burgers equation, pressure will be removed from this derivation. This simplification means we are free to proceed to the reconstruction of non-linear/convective

term. This term is more mathematically involved and thus the following derivation will be more explicit.

Firstly the non-linear term is rearranged in the following manner:

$$u(x)_j \frac{\partial u(x)_i}{\partial x_j} = \frac{\partial u(x)_j u(x)_i}{\partial x_j} = \frac{\partial}{\partial x_j}(u(x)_j u(x)_i)_F \tag{2.18}$$

Understanding that

1. The spatial derivative, $\frac{\partial}{\partial x_j}$, of the Fourier transformation yields an additional ik term as it did in the viscous term and
2. That the subscript $_F$ denotes the need to conduct a Fourier transformation

the following equation can be created.

$$\frac{\partial}{\partial x_j}(u(x)_j u(x)_i)_F = ik(\sum_{k'}^{\infty} \hat{u}(k') e^{ik'x} \sum_{k''}^{\infty} \hat{u}(k'') e^{ik''x})_F \tag{2.19}$$

With some rearrangement and combination of the exponential terms, Eq. 11. can be simplified further into Eq. 12.

$$\frac{\partial}{\partial x_j}(u(x)_j u(x)_i)_F = ik(\sum_{k'}^{\infty} \sum_{k''}^{\infty} \hat{u}(k') \hat{u}(k'') e^{ix(k'+k'')})_F \tag{2.20}$$

It should be noted that Eq. 12 is still expressed in physical space of the flow and has yet to be transformed to the spectral space. To do this Eq. 12 must be multiplied by a

factor of e^{-ikx} and volume averaged over the entirety of physical space. This results in the creation of Eq. 13, for the readers convenience the left hand side will no longer be written down as all further operations will be confined to the right hand side.

$$< ik(\sum_{k'}^{\infty}\sum_{k''}^{\infty}\hat{u}(k^{'})\hat{u}(k^{''})e^{ix(k^{'}+k^{''}-k)}) > \tag{2.21}$$

Since the velocity amplitudes $\hat{u}(k^{'})$ & $\hat{u}(k^{''})$ are not a function of space the volume averaging operation can be confined to the exponential term $< e^{ix(k^{'}+k^{''}-k)} >$. It is at this point we invoke the properties of the Dirac delta function, shown below, in order to get the final form of the non-linear term in spectral space.

The Dirac delta function is formally defined as follows:

$$\delta(x-a) = \frac{1}{2\pi}\int_{-\infty}^{\infty} e^{ip(x-a)}dp \tag{2.22}$$

The properties of this function are listed below.

1. $\delta(x) = +\infty, x = 0$
2. $\delta(x) = 0, x \neq 0$

Most importantly, however, is the value of the delta function when it is integrated across the entirety of the domain.

3. $\int_{-\infty}^{\infty} \delta(x)dx = 1$

Understanding that $\delta(x-a)$ is in fact $\delta(k^{'} + k^{''} - k)$ and as such $(k^{'} + k^{''} - k) = 0$ the index $k^{''}$ can be expressed in terms of $k^{'}$ & k in the following manner $k^{''} = k - k^{'}$. Applying this fact in conjunction with the above rules yields Eq. 14.

$$u(x)_j \frac{\partial u(x)_i}{\partial x_j} = ik_m \sum_{k^{'}}^{\infty} \hat{u}(k^{'})\hat{u}_m(k - k^{'}) \tag{2.23}$$

Now that all three terms in the viscous Burgers' equations have been developed, they can be listed together in Eq. 15.

$$\frac{\partial \hat{u}(k)}{\partial t} + ik_m \sum_{k^{'}}^{\infty} \hat{u}(k^{'})\hat{u}_m(k - k^{'}) = \frac{-k^2}{Re}\hat{u}(k) \tag{2.24}$$

To further simplify Eq. 15. it is suggested that the non-linear term be moved to the right hand side, while the viscous term is brought to the left hand side. The simplification of Eq. 15. yields the final simplified form of the spectral viscous Burgers' equation shown below.

$$(\frac{\partial}{\partial t} - \frac{k^2}{Re})\hat{u}(k) = -ik_m \sum_{k^{'}}^{\infty} \hat{u}(k^{'})\hat{u}_m(k - k^{'}) \tag{2.25}$$

Now that the Burgers equation has been converted into spectral form it is easier to make sense of what each of the terms contributes to turbulence as a whole. Looking first at the non-linear convective term, its job is the production of new, smaller waves of larger wave-number. It take large mean flow scaled waves and creates from it smaller and smaller scaled waves. The role of viscosity becomes clear with the above spectral description of the flow. As the Reynolds number increases so to does the wave-number. The action of viscosity is also proportional to wave-number squared, which means that viscosity acts much more intensely on smaller sized waves, larger wave-numbers.

While these descriptions of the flow are useful in helping understand the nature of turbulence, solving these equations are incredibly computationally expensive. The expense of the problem scales as a function of the Reynolds number cubed. Solving these equations, in the DNS framework, would be incredibly expensive. In an attempt to get an acceptably accurate solution, with limited computational resources, the use of turbulence models is employed.

2.3 CFD Code and Simulation Methodology

As previously mentioned, the computational cost of direct numerical simulations scales with the Reynolds number cubed. A frightening prospect if one is looking to conduct DNS simulations of more practical engineering domains. In an attempt to reduce the required computational resources it was decided that the cold-leg mixing experiment would be simulated using Siemen's Star CCM+.

The work flow within CCM+ is relatively simple and straightforward. The processes required to get a simulation running in CCM+ is as follows:

1. A geometry must be created either through the Star CCM+ CAD tool or 3rd party software.
2. The mesh continua must be established.
3. Establish the physics continua.
4. Apply all relevant boundary and initial conditions.
5. Select the simulation stopping criteria.
6. Create derived parts at locations of interest within the domain
7. Selected monitoring criteria at locations of interest

In this thesis the solid geometry of the experimental setup was created by the experimental group using SolidWorks. Using SolidWorks the interior volume was extracted and post processed in order to align with the constraints of the problem and desired boundary and operating conditions. The geometry will be discussed in more detail in a dedication portion of this thesis.

In any CFD simulation the generation of a mesh is one of the most difficult parts of the work-flow. This is because mesh generation requires the user to make several a priori assumptions about the behavior of their system in order to accurately generate a mesh. This of particular importance in this case as it is a highly transient, multi-regime natural convection flow. What may constitute as adequate mesh refinement in the cold-leg of this geometry might not suffice in the down-commer region where the fluid is accelerating and the y+ values are larger. The mesh characteristics will be discussed in more detail in a dedication portion of this thesis.

2.3.1 Physics Continua & Turbulence Model

At the time these simulations were being created, the experimental setup was undergoing many changes both in geometry and material properties. with that in mind it should be recognized that the simulations conducted within this thesis are preliminary in nature an were designed to help guide the experimentalists in selecting relevant comparison criteria for the V&V benchmark.

For the turbulence model the K-Epsilon formulation was used, see Eq. 2.26 & 2.32 below.

$$\frac{\partial}{\partial t}(\rho k) + \nabla \bullet (\rho k \bar{v}) = \nabla[(\mu + \frac{\mu_t}{\sigma_k})\nabla k] + P_k - \rho(\epsilon - \epsilon_0) + S_k \tag{2.26}$$

$$\frac{\partial}{\partial t}(\rho \epsilon) + \nabla \bullet (\rho \epsilon \bar{v}) = \nabla[(\mu + \frac{\mu_t}{\sigma_\epsilon})\nabla \epsilon] + \frac{1}{T_e} C_{\epsilon 1} P_\epsilon - C_{\epsilon 2} f_2 \rho(\frac{\epsilon}{T_e} - \frac{\epsilon_0}{T_0}) + S_\epsilon \tag{2.27}$$

Where P_k is defined as:

$$P_k = G_k + G_b \tag{2.28}$$

And P_ϵ is defined as:

$$P_\epsilon = G_k + C_{\epsilon 3} G_b \tag{2.29}$$

Where G_k is the turbulent production term which is defined as:

$$G_k = \mu_t S^2 - \frac{2}{3}\rho k \nabla \bullet \bar{v} - \frac{2}{3}\mu_t (\nabla \bullet \bar{v})^2 \tag{2.30}$$

Where G_b, most importantly, is buoyant turbulent production term and its definition is as follows.

$$G_b = \beta \frac{\mu_t}{Pr_t} (\nabla \bar{T}) \bullet g) \tag{2.31}$$

From Eq. 2.29 it should be noted that the constant $C_{\epsilon 3}$ is defined as:

$$C_{\epsilon 3} = Tanh \frac{|V_b|}{|U_b|} \tag{2.32}$$

From this point it is appropriate to discuss how the treatment of the walls were handled. In this study, given its preliminary nature, it was decided that the wall function that offered the greatest range of operable y+ values would be utilized. The wall treatment selected is known as the Two Layer Formulation, the particular flavor utilized in this thesis was the buoyant formulation by Xu et al. [16]. The reasoning behind its selection was the fact that it could handle meshes with an approximate y+ around 1 as well as meshes with y+ bounded as follows 30<y+ 1<100.

The equation that governs the two-layer formulation is listed below in Eq. 3.33 & 3.34

$$\epsilon = \frac{k^{(\frac{3}{2})}}{l_\epsilon} \tag{2.33}$$

where l_ϵ is defined as follows:

$$l_\epsilon = \frac{8.8d}{1 + \frac{10}{y_v^*} + 5.15x10^{-2} * y_v^*} * \frac{1}{\sqrt{\frac{\bar{v}^2}{k}}} \tag{2.34}$$

2.3.2 Boundary Conditions

The Boundary conditions for this domain are quite simplistic. The cold-leg mixing experiment, as well as the scoping simulations, are a closed system. Therefor there are no inlets and outlets, only walls. Thus all boundary related phenomena are handled by the two-layer formulation near the wall

2.3.3 Initial Conditions

Being a closed and transient system means that the initial conditions are all that more important. Selection of velocities and turbulent quantities are simple, as they are initialized to zero or near zero amounts. the difficulty lies with the molecular diffusion term and how to treat it. Literature suggests, [17] [18] [19] that a turbulent Schmidt number be set near unity. This assumption implies that the turbulent viscosity and the turbulent mass diffusivity are equivalent. Regarding the molecular Schmidt number the same literature suggested, for salt-water and deionized water mixtures, a Schmidt number of 1000 - 2100 be utilized. There isn't a lot of clarity regarding the specifics of choosing a Schmidt number from literature so for this investigation a value of 1000 was chosen.

2.3.4 Selected Numerical Methods for CFD

For the sake of reducing the computational cost of the simulations a segregated flow solver was utilized. This had the intended effect of making individual iterations mush quicker, however overall convergence was markedly slower once the mesh sizes started increasing.

Table 2.1: Table containing the numerical methods used for the cold-leg mixing simulation

	Method
Spatial Discretization	2nd order upwind
Temporal Discretization	2nd order implicit
Multi-Component Liquid	2nd order convective
Time Step	5.0e-5s, 2.5e-5 s
Solver	Segregated Pressure Algorithm
Pressure Correction	SIMPLE

2.3.5 Material Properties for Physics Continua

The material properties used for the initial simulations are listed below in table 2.2. These properties were used for early experimental shakedown runs which were targeting an approximate 10% density difference between the two fluids.

Table 2.2: Table of material properties for CFD simulations

Fluid Property	Value	
	Heavy Fluid	Light Fluid
Fluid	Salt Water Mixture	DI-Water
Density	1028.5 Kg/m^3	924.29 Kg/m^3
Dynamic Viscosity	.001135 Pa-s	.002273 Pa-s
Density Difference	104.21 Kg/m^3	

2.4 Grid Convergence Index

In order to calculate the uncertainties associated with the discretization of the computational domain the Grid Convergence Index (GCI) method, presented in Celik et al. [20], will be utilized. The method is base on the principle of Richardson extrapolation and has been utilized in a litany of CFD publications. The procedure consists of five simple steps:

1. Define a representative grid-cell size for the one, two or three dimensional case

   For one dimensional cases:

   $$h = \frac{1}{n}\sum_{i=1}^{N} \Delta L \tag{2.35}$$

   For two dimensional cases:

   $$h = (\frac{1}{n}\sum_{i=1}^{N} \Delta A)^{\frac{1}{2}} \tag{2.36}$$

   For three dimensional cases:

   $$h = (\frac{1}{n}\sum_{i=1}^{N} \Delta V)^{\frac{1}{3}} \tag{2.37}$$

2. Create three separate grids that have a refinement factor of approximately 1.3

   The refinement factor r is defined as follows:

   $$r = \frac{h_{coarse}}{h_{fine}} \tag{2.38}$$

3. With some constraints on the values of h_1, h_2 & h_3

   where:

   $$h_1 < h_2 < h_3 \tag{2.39}$$

and the definition of the refinement factors between the fine and medium grids and the medium and coarse grids as

$$r_{21} = \frac{h_2}{h_1} \tag{2.40}$$

$$r_{32} = \frac{h_3}{h_2} \tag{2.41}$$

the apparent order of the numerical method, p, can be defined in with the following formulations:

$$p = \frac{1}{ln(r_{21})}|ln|\frac{r_{32}}{r_{21}}| + q(p)| \tag{2.42}$$

Where $q(p)$ is defined as:

$$q(p) = ln(\frac{r_{21}^p - s}{r_{32}^p - s}) \tag{2.43}$$

Where s is defined as:

$$s = 1 \bullet sgn(\frac{\epsilon_{32}}{\epsilon_{21}}) \tag{2.44}$$

It should be noted that ϵ is defined as the following:

$$\epsilon_{32} = \phi_3 - \phi_2 \tag{2.45}$$

$$\epsilon_{21} = \phi_2 - \phi_1 \tag{2.46}$$

Where phi is the quantity of interest that the uncertainties are being appended to. It should be noted that the apparent order p is solved using fixed point iterations, where $q(p) = 0$ when $h =$ some constant.

4. Step four involves calculating the extrapolated values for phi in the following manner:

$$\phi_{ext}^{21} = \frac{(r_{21}^{p}\phi_1 - \phi_2)}{(r_{21}^{p} - 1} \tag{2.47}$$

5. Report on the values of the approximate relative error and the extrapolated relative error and the apparent order of magnitude.

$$e_a^{21} = |\frac{\phi_1 - \phi_2}{\phi_1}| \tag{2.48}$$

$$e_{ext}^{21} = |\frac{\phi_{ext}^{12} - \phi_1}{\phi_{ext}^{12}}| \tag{2.49}$$

$$GCI_{fine}^{21} = \frac{1.25e_a^{21}}{(r_{21}^{p} - 1} \tag{2.50}$$

The values of the GCI_{fine}^{21} are overlayed on top of the figure on which uncertainties are being calculated. The error bars accompanying the majority of the results section are calculated utilizing this procedure.

3. EXPERIMENTAL AND SIMULATED GEOMETRY

3.1 Experimental Geometry

The 5^{th} benchmark of CFD applications to nuclear reactor safety, approved by the Committee on the Safety of Nuclear Installations (CSNI), focuses on the cold-leg mixing characteristics of PWR-like geometry. The construction and operation of the facility was conducted at TAMU and it is comprised of three main parts. A CAD drawing of the experimental facility, provided by [21], can be seen below in Figure 3.1. The heavy fluid tank, on the left, contains a saltwater mixture which is connected via the cold-leg to a light fluid tank, on the right, which is filled with a mixture of de-ionized water and ethanol.

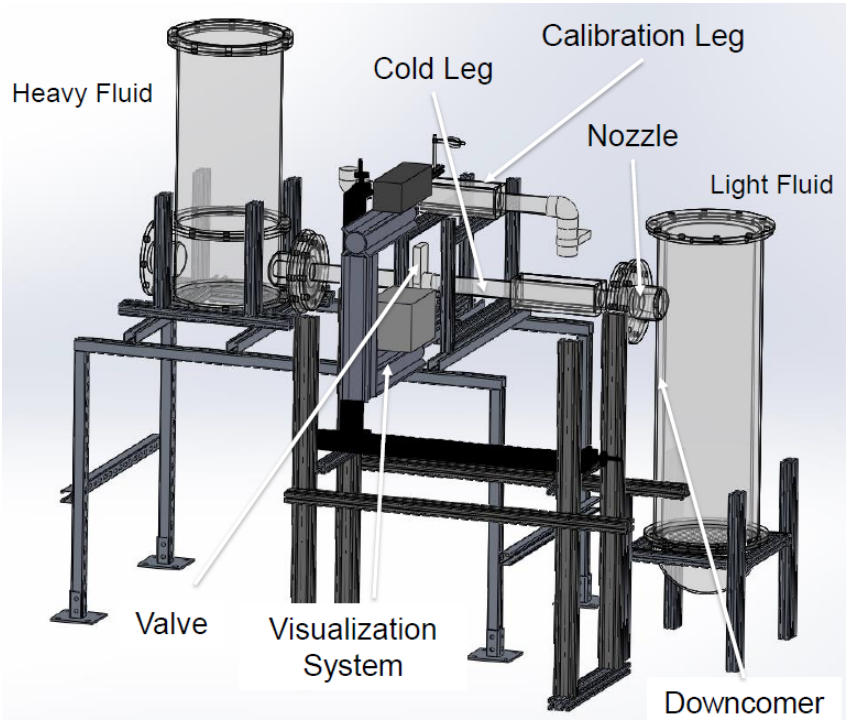

Figure 3.1: CAD drawings of the experimental facility. Reprinted from [21]

Special attention has been given to the nozzle leading into the downcommer region. Displayed in Figure 3.2 is a diagram of this nozzle, its design was provided by Electricite de France (EDF) and manufactured by the TAMU nuclear engineering thermal hydraulics group. It should be noted that due to the complexity, cost of manufacturing and experimental focus the nozzle was only implemented on the light-fluid side of the experiment. The nozzle on the heavy-fluid side of the experimental facility features a bluff nozzle, as opposed to the curved EDF nozzle.

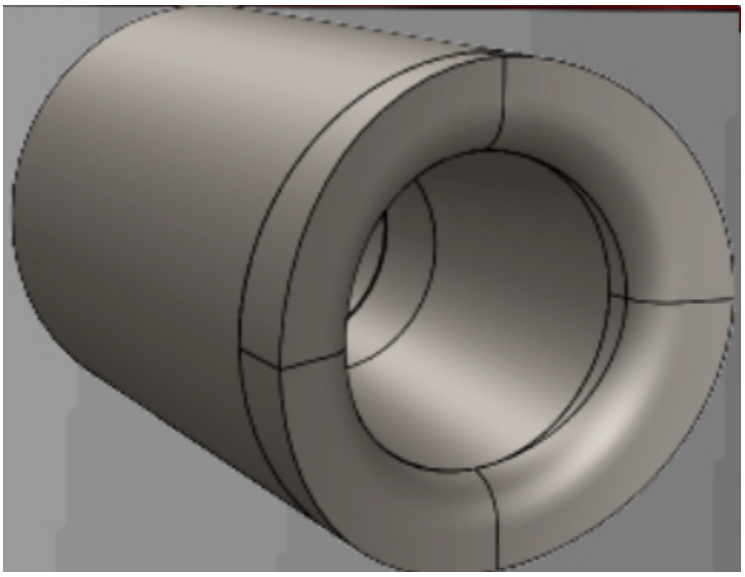

Figure 3.2: CAD drawing of the nozzle provided by Electricite de France

Shown below, in Figure 3.3, is a view of the interior fluid volume focused in on the lower portion of the light-fluid tank. In order to reduce the cost associated with each experimental test, a gasket was inserted into the light-fluid tank in order to reduce its overall volume. The gasket has a similar impact on the simulations as well. With the reduction in fluid volume comes a reduction in the number of nodes required in the domain of interest, thus reducing the computational cost of each simulation while increasing the speed at which it runs on a consistent allotment of core-hours. One difficulty associated with the gasket is its introduction of curvature to the bottom of the light-fluid tank. This curvature was disregarded in the simulations and the bottom of the simulated domain was taken to be flat.

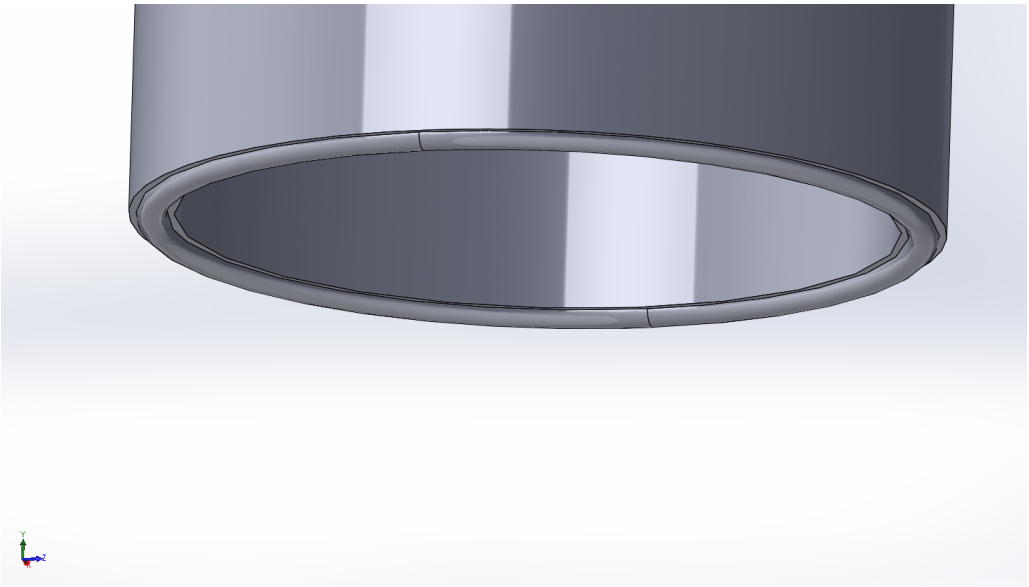

Figure 3.3: Interior fluid volume detailing the position and shape of the gasket

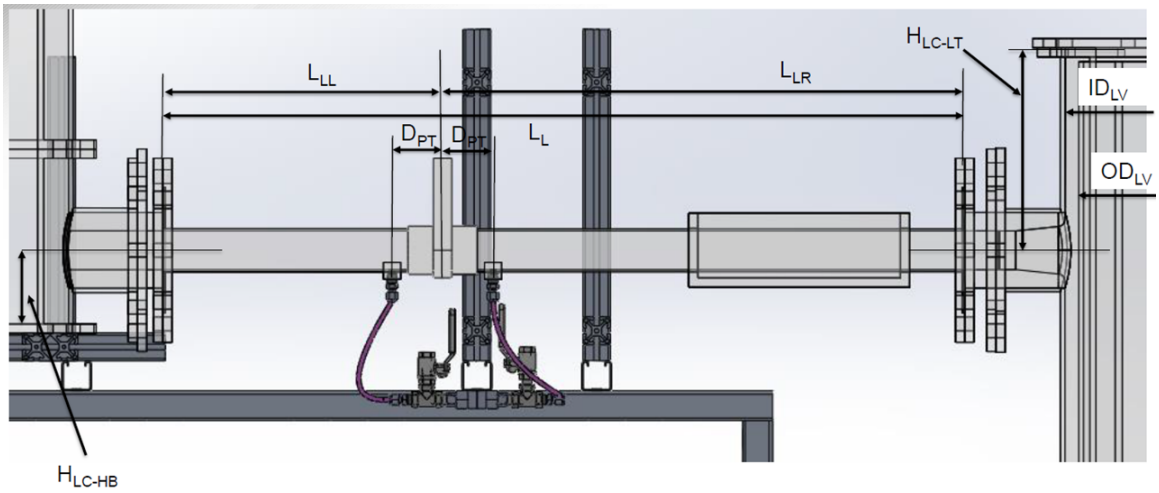

Figure 3.4: Early technical drawing of the cold-leg mixing experiment

3.2 Simulated Geometry, Interior Fluid Volume

The volume of interest, in regards to the simulations, is presented below in Figure 3.4 the right portion of the presented volume represents the heavy fluid tank and the height of this volume must be adjusted in order to satisfy the a particular boundary condition. This condition, in order to isolate the effects of buoyancy, requires that the hydrostatic pressure be equivalent across the knife-valve. As the density difference between the two fluids approaches zero, the height of the heavy fluid tank approaches the height of the light fluid tank.

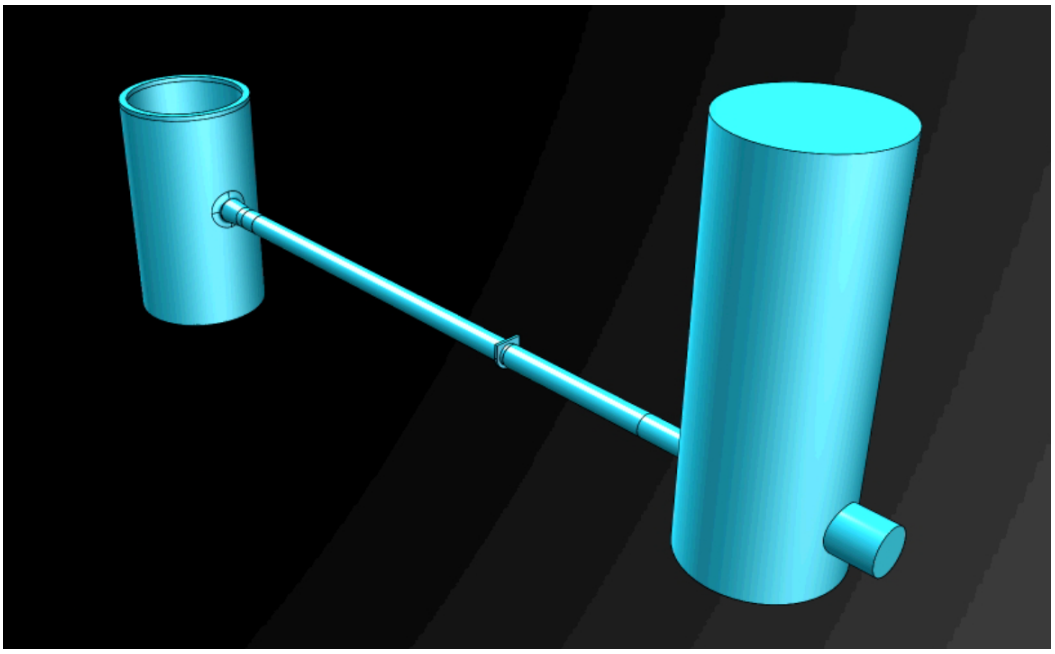

Figure 3.5: Solidworks extraction of unadjusted interior fluid volume [21]

Shown below, in Figure 3.5, is the knife-valve which initially separates the two fluid mixtures. Of particular importance is the boundary condition that controls the hydrostatic pressure across this valve. As mentioned earlier, the hydrostatic pressure across the knife-valve needs to be zero in order to isolate the effects of buoyancy on the system. This is done by using the formulation in equation 3.1 to control the height of the heavy fluid tank.

$$h_{heavy} = h_{light} * \frac{\rho_{light}}{\rho_{heavy}} \tag{3.1}$$

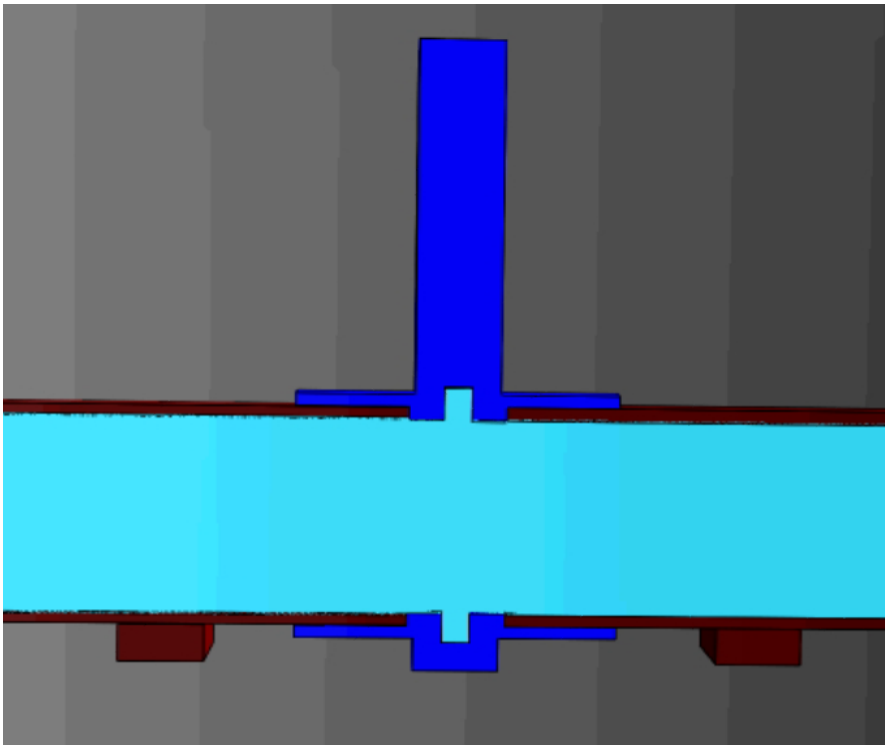

Figure 3.6: CAD drawing of the knife-valve used to initially separate the two fluid mixtures

3.3 Domain Simplifications and Difficulties

In order to reduce the computational cost and overall complexity of the simulations several simplifications to the system were made. In the experiment, on the heavy-fluid tank, the upper surface of the fluid column was always exposed to a free surface. This is because the height of the heavy fluid column was constantly changing as a function of the experimental density differences between the two fluids. This free surface, in all simulations, was neglected and instead replaced with a wall boundary.

In order to reduce the complexity of the simulation's geometry and initialization, multiple assumptions were applied with respect to the knife valve. The action of opening the valve was neglected. This action was neglected because of the cost associated with mesh deformation studies and the limited availability of computational resources. This assumption was initially justified for two reasons.

1. The distance between the knife-valve and the first particle image velocimetry (PIV) window was considered sufficiently large thus providing ample length for any fluid impacts to be dampened out.

2. The valve was reported to open in approximately 25 milliseconds. Which for the smallest time step size, $2.5E^{-4}$ seconds, only amounted to 100 timesteps where mesh deformation was occurring.

The second valve simplification involved modifying the fluid geometry of the valves' open state. This can be visualized by looking at Figure 3.6 which is shown below.

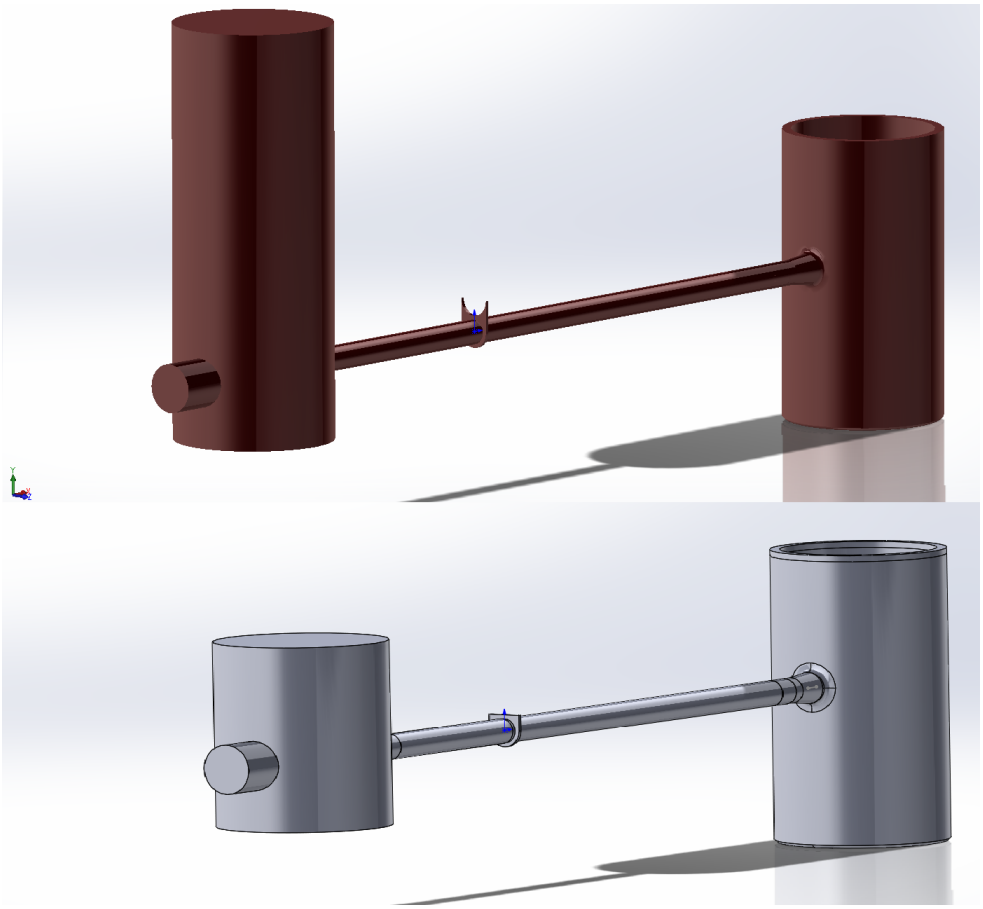

Figure 3.7: Comparison of the unedited, pre-simplification, and the edited, post simplification, fluid volumes

3.4 Meshing and Mesh Characteristics

During the initial scoping phase of the experimental analysis the geometry was subject to rapid change and variation in its complexity. Several variations on the experimental geometry are discussed below.

1. Initially, as shown below in figure 3.7, the length of the transfer-pipe was much shorter. Additionally the overall height of the light fluid tank was much larger.

2. It was a possibility for a while that the lower plenum might be considered in the experimental analysis as well as a mesh grid. This meant not only would the lower plenum need to be included in CFD calculations but also the interior core of the reactor. This would have greatly increased the scope and computational cost of the accompanying CFD simulations.

3. Due to the cost of the hot / light fluid, which was an ethanol water mixture, efforts to reduce the volume of the hot leg of the test section were undertaken. The primary result of this effort was the inclusion of a gasket to help minimize the volume.

Because of these rapid variations in the experimental geometry it was decided that, for preliminary-guiding simulations, the mesh type used would be of the unstructured hexahedral variety. The primary benefit associated with this mesh type is that software, either ANSYS: ICEM or the Siemen's Star CCM+ meshing tool, can readily automatically generate an unstructured hexahedral mesh given a geometry input file. These software packages are decent at generating meshes for complex geometries, however they are often more computationally expensive. This is because a structured hexahedral block mesh is capable of meshing a geometry with a lower number of nodes.

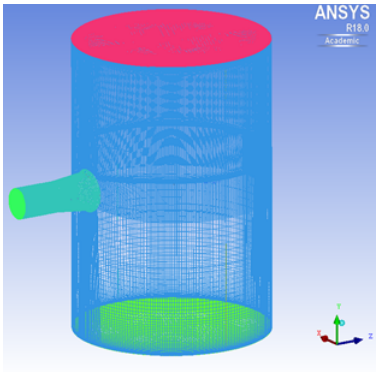

Figure 3.8: Initial Cold-leg mixing hexahedral mesh configuration

Table 3.1: Mesh Characteristics for the Course, Medium and Fine Mesh Simulations

	Coarse	Medium	Fine
Number of Cells	1,053,158	3,222,966	9,875,255
Max wall y+	2.979	1.77	1.24
Max Skewness Angle	76.28	83.46	83.86
Mesh Type	Hexahedral	Hexahedral	Hexahedral
Time Step	5.0E-4	5.0E-4	2.5E-4
Maximum CFL	.668	.635	.725
Length Characteristic	.0037 m	.0025 m	.0018
Mesh Refinement Factor	N/A	1.4518	1.4524

The mesh utilized in the simulation displayed in Figure 3.7 was a structured hexahedral block mesh, at the time it was believed that the geometry would undergo no further changes. However once the light fluid was switched from deionized water to the ethanol water mixture the geometric variations started to manifest. Shown below, in figure 3.8, is the surface mesh of the EDF nozzle utilized in the first structured mesh simulation. Shown below in Figures 3.9 & 3.10 are the visualizations of the medium sized unstructured meshes in the heavy tank region and EDF-nozzle region of the simulation domain.

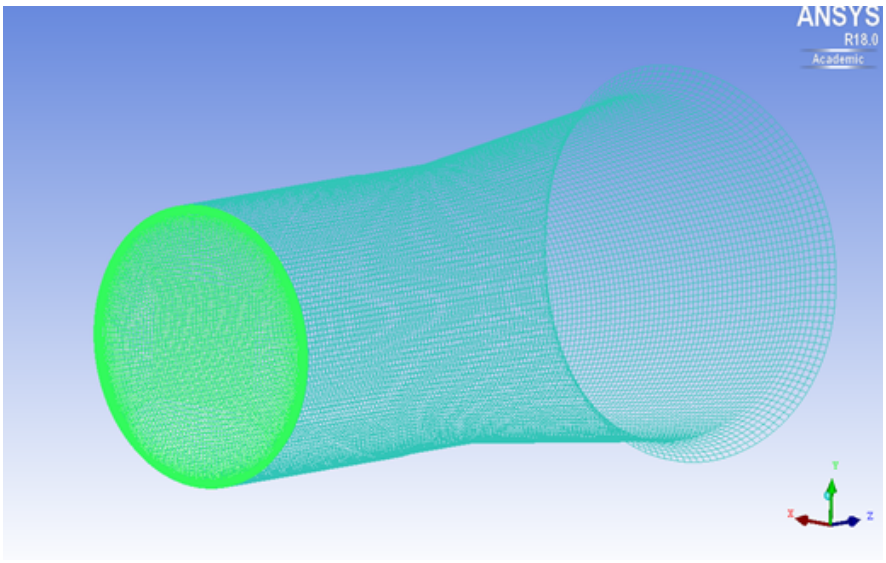

Figure 3.9: Initial Cold-leg mixing surface mesh of EDF nozzle

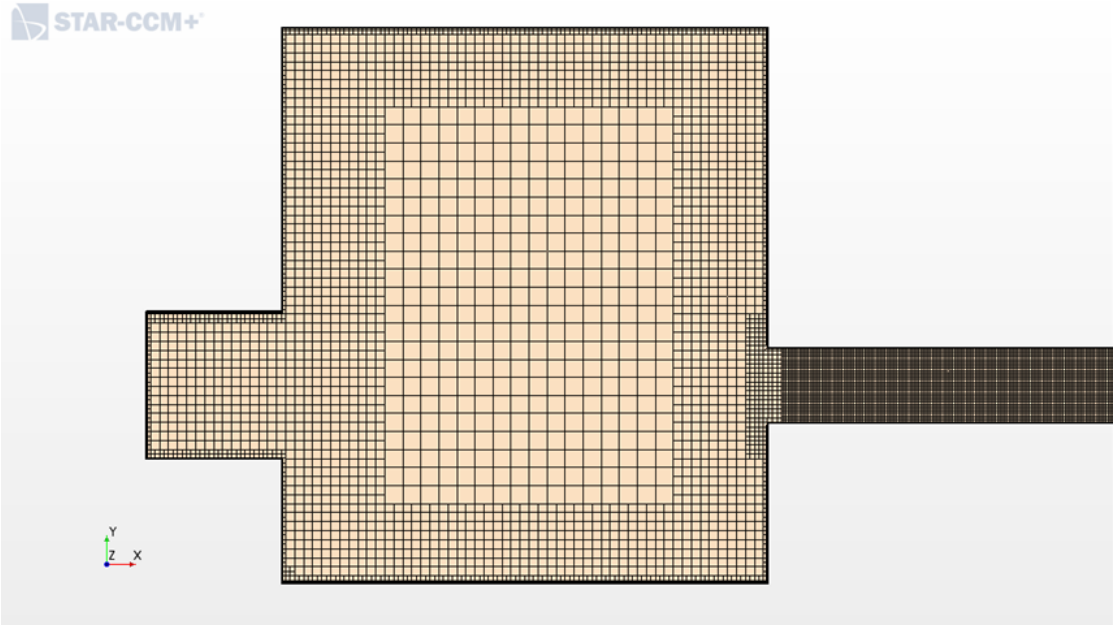

Figure 3.10: Visualization of unstructured interior mesh of the medium mesh case in the heavy fluid region of the experiment.

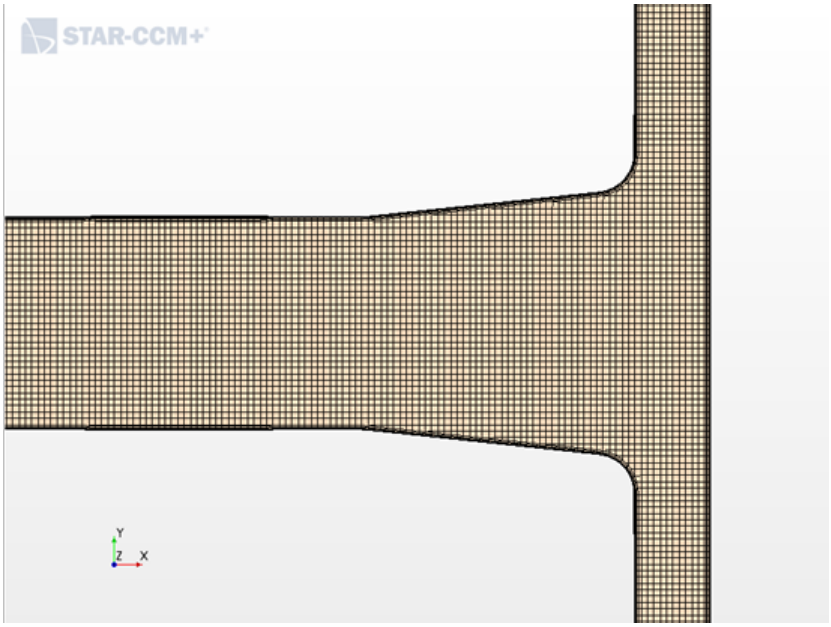

Figure 3.11: Visualization of unstructured interior mesh of the medium mesh case in the EDF-nozzle region of the experiment.

4. RESULTS

4.1 Deviation between Experimental and Computational Material Properties

Given the preliminary nature of the initial experiments and simulations a multitude of line probes were placed throughout the entirety of the domain in the hopes that a couple would be located within an experimental particle image velocimetry windows. For this reason the results presented herein are of simple line probes placed set distances away from each other. Additionally, due to the rapidly changing experimental parameters, it should be noted that the materials properties for the initial simulation differed by approximately 3.5-7.2 percent depending on the fluid property being inspected. See figures 4.1-4.3 below.

Table 4.1: Table Detailing the CFD Material Properties

	CFD Fluid Properties	
	Heavy Fluid	Light Fluid
Fluid	Salt Water Mixture	DI-Water
Density	1028.5 Kg/m^3	924.29 Kg/m^3
Dynamic Viscosity	.001135 Pa-s	.002273 Pa-s
Density Difference	104.21 Kg/m^3	

Table 4.2: Table Detailing the Experimental Material Properties

	Experimental Fluid Properties	
	Heavy Fluid	Light Fluid
Fluid	Salt Water Mixture	Ethanol-Water Mixture
Density	1064.7 Kg/m^3	956.54 Kg/m^3
Dynamic Viscosity	.00109 Pa-s	.00245 Pa-s
Density Difference	108.16 Kg/m^3	

Table 4.3: Table showing the Differences in Material Property Values between the Experiment and Simulation

	Difference Between CFD and Experimental Material Properties	
	Heavy Fluid	Light Fluid
Density	3.4%	3.4%
Dynamic Viscosity	4.1%	7.2%
Density Difference	3.7%	

4.1.1 Locations of Interest and Opening Statements

Of the multitude of line probes placed within the domain, only four managed to coincide with the experimental measurement window. These lines, referred internally as vertical line (VL) 1, VL 4, horizontal line (HL) 7 & HL 12, were placed with the intent of capturing the transient nature of the flow near the initial valve location and the downcommer regions of the reactor vessel. Only the values of velocity and density were reported on the various line probes within the domain. It should also be noted that while some reports show instantaneous developmental profiles, the majority of the results are of time averaged values whose ranges will be discussed later in the thesis.

In any study involving turbulent flows, plotting higher order statistics and turbulent parameters would be mandatory. However, due to the preliminary of nature of the conducted simulations and a couple of revelations which will be discussed in the conclusions, it was determined this type of analysis was premature

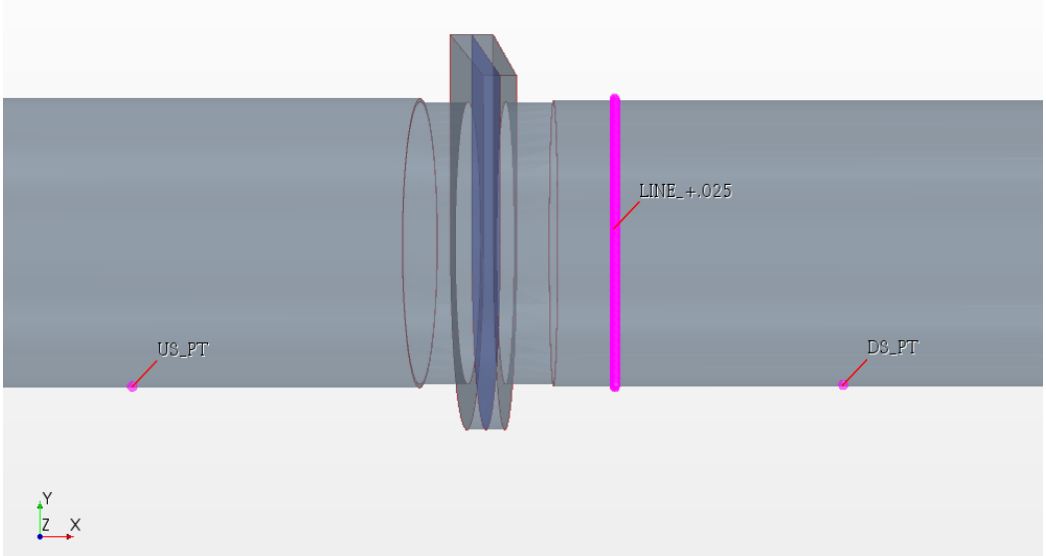

Figure 4.1: Visualization of Vertical Line 1. This line is located close to the initial knife valve separating the domain.

4.1.2 Results on Vertical Line 1 and Initial Pressure Tap Reading

The primary reasoning behind putting the first line so close to the initial valve was the desire to track the initial development of the fluid front. Primarily with the hopes of better characterizing the impact the valve has on the overall flow. Additionally it was desired that a line probe be place in between the two pressure taps. A visualization of the line probe and the two pressure taps can be seen below in figure 4.1.

Looking at figures 4.2 - 4.5 the pressure difference between the upstream and downstream taps can be seen as a function of time. In the first 2 seconds a pressure spike, seen more resolutely on figure 4.3, likely attributed to the flow hitting the surface of the taps, is recorded and quickly begins to decay. At this point in time the three meshes perform similar to each other, with the fine mesh under-predicting the pressure drop across the two taps. Moving on to figure 4.4 the same pressure signal can be seen for the time frame of 10 through 35 seconds.

The previous trend, the fine mesh under-predicting the pressure drop, seems to continue throughout this time series. The coarse and medium meshes seem to oscillate between being greater than or less than each other. The general behavior of the pressure drop is still tending downwards. Looking at figure 4.5 the remainder of the time signal can be seen, 35-90 seconds. Unfortunately, due to the excessive computational cost and lack of available resources, the fine mesh wasn't able to continue producing data in this time range. The average behavior of the pressure drop has the medium refinement mesh over-predicting the pressure drop when compared to its coarse counterpart.

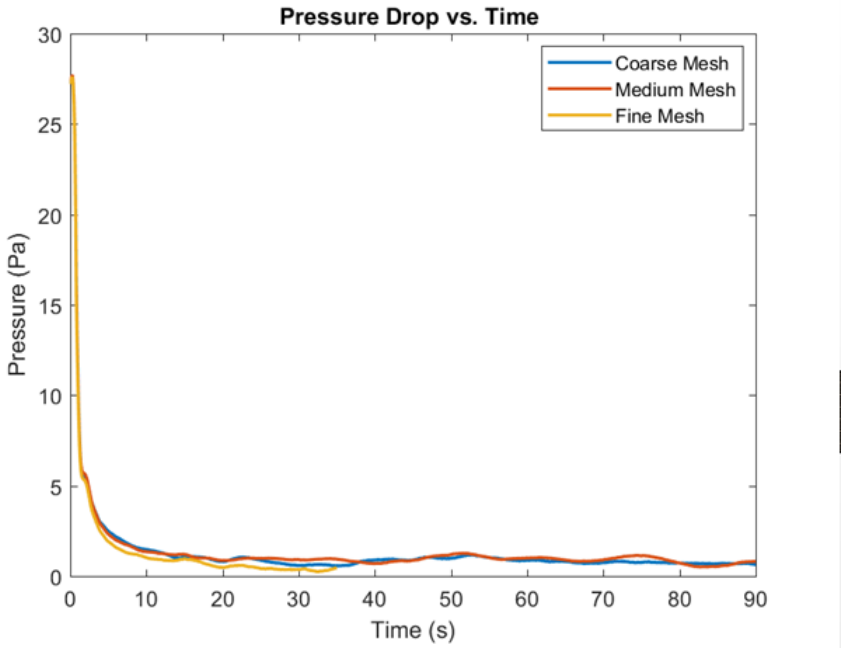

Figure 4.2: Pressure drop signal for entire time series

Continuing on to figures 4.6 & 4.7 the developmental density and velocity profiles can be seen. The development of the x-velocity and density profiles occurs within roughly .33 seconds. For the readers reference a dot has been placed on each time's corresponding line to indicate the location of the maximum value as time progresses. The high density fluid, flowing from the left of the graph towards the right, posses a higher velocity and is confined to a smaller cross-section of the pipe at this location in the cold-leg. This is due to the knife valve location not being located at the center of the cold leg, the effect is that the density and velocity profiles are not entirely symmetric.

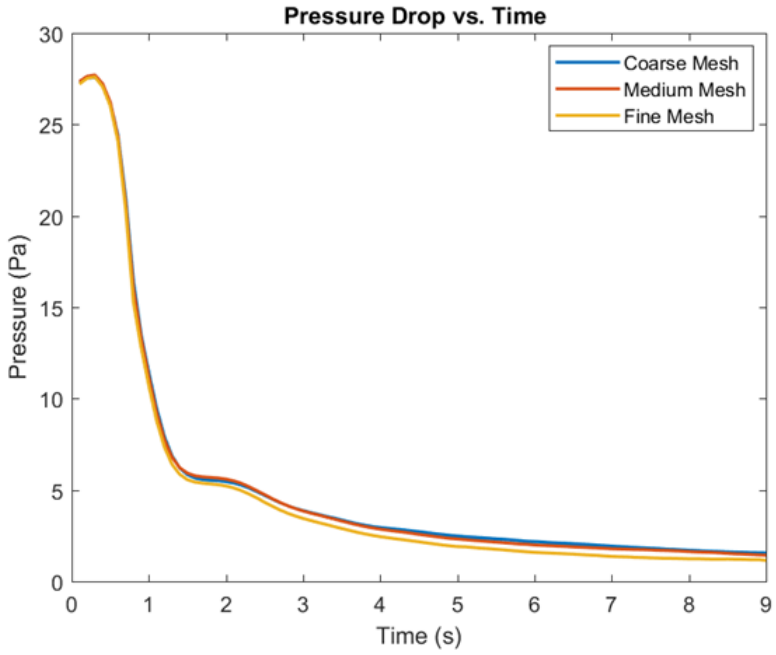

Figure 4.3: Pressure drop signal for 0-9 second time range

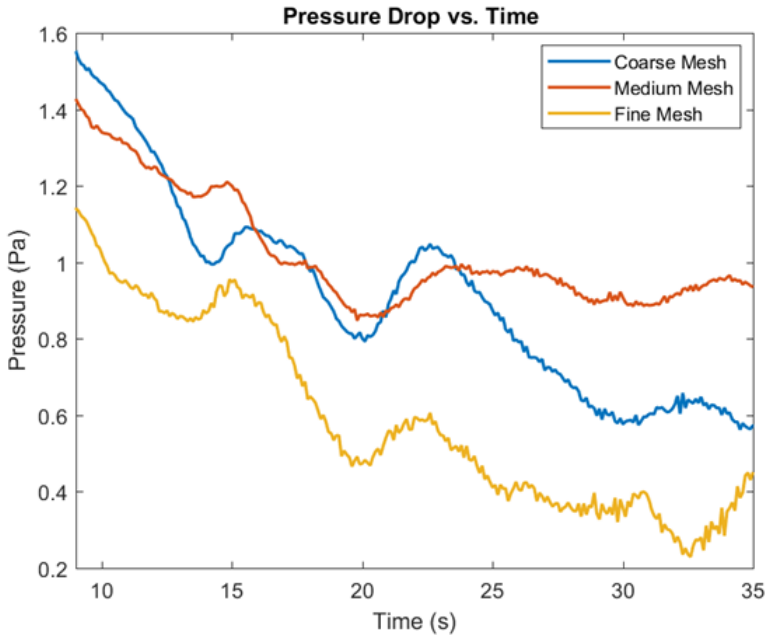

Figure 4.4: Pressure drop signal for 10-35 second time range

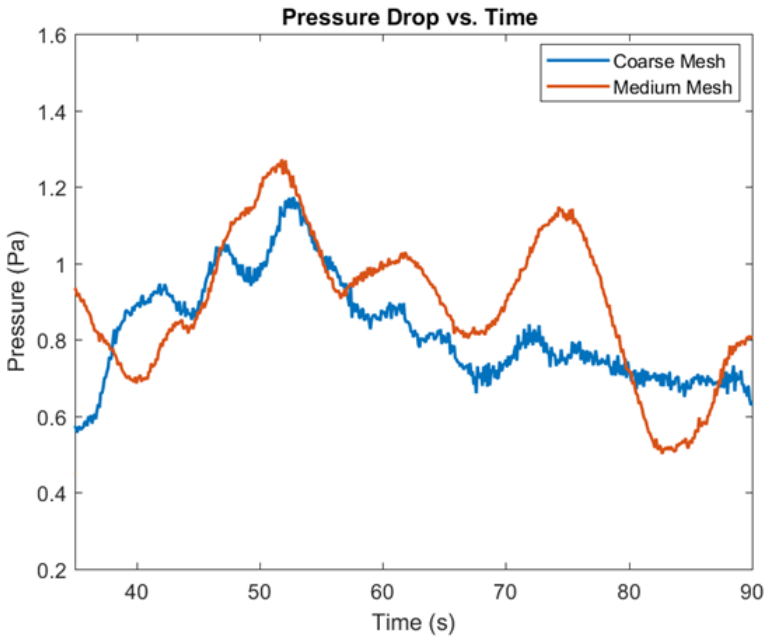

Figure 4.5: Pressure drop signal for 35-90 second time range

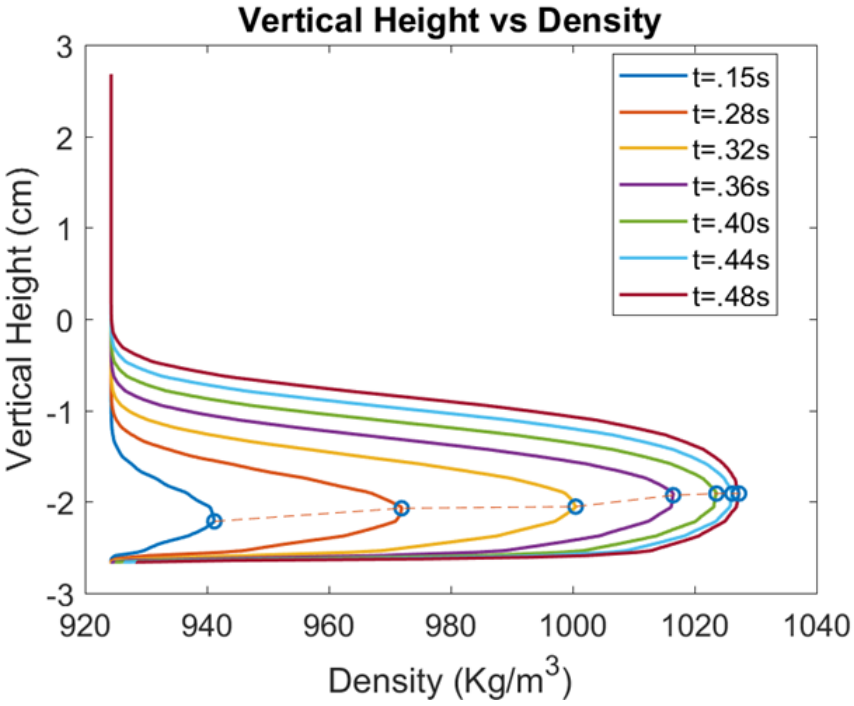

Figure 4.6: Developmental density profiles on a vertical trace near the valve

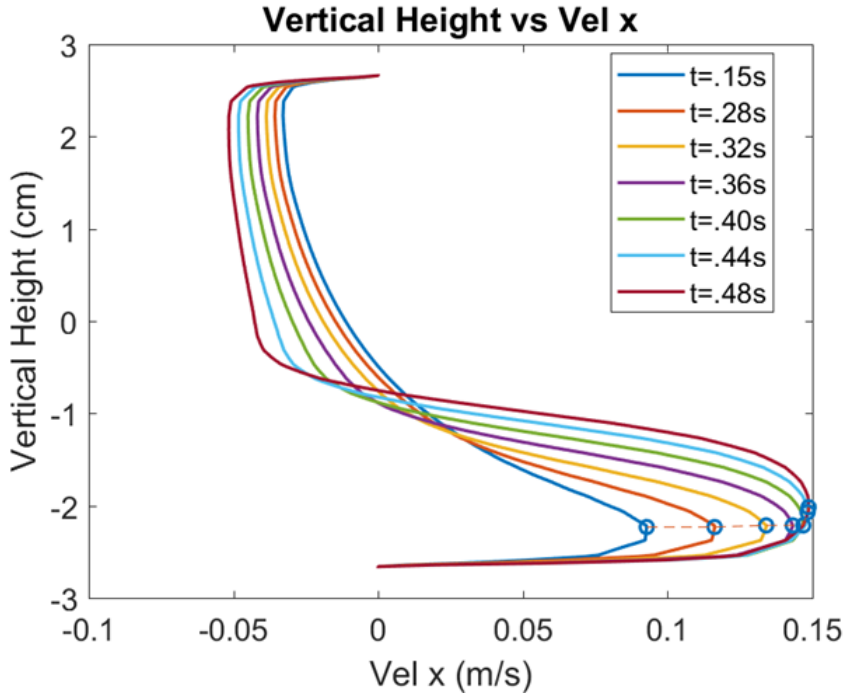

Figure 4.7: Developmental velocity profiles on a vertical trace near the valve

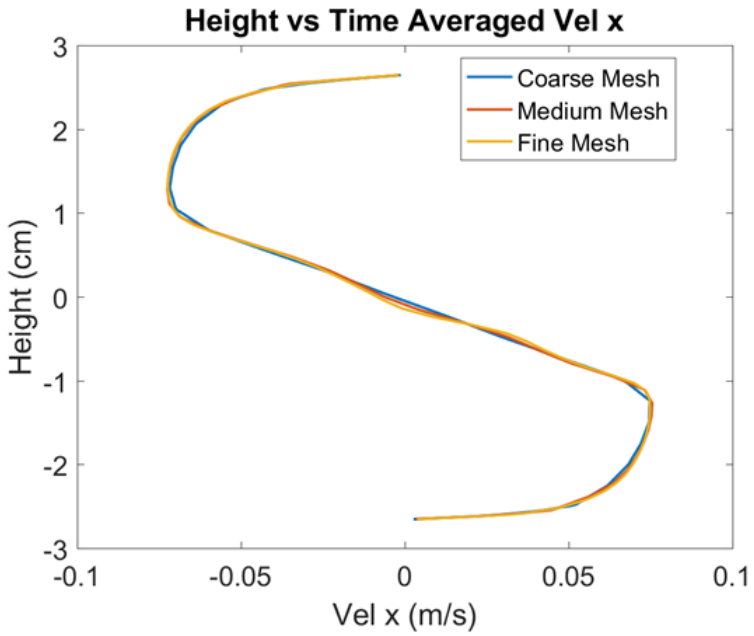

Figure 4.8: Time averaged velocity profiles of the coarse, medium and fine meshes for the time range of $6.38 - 16.38$ seconds on vertical line 1

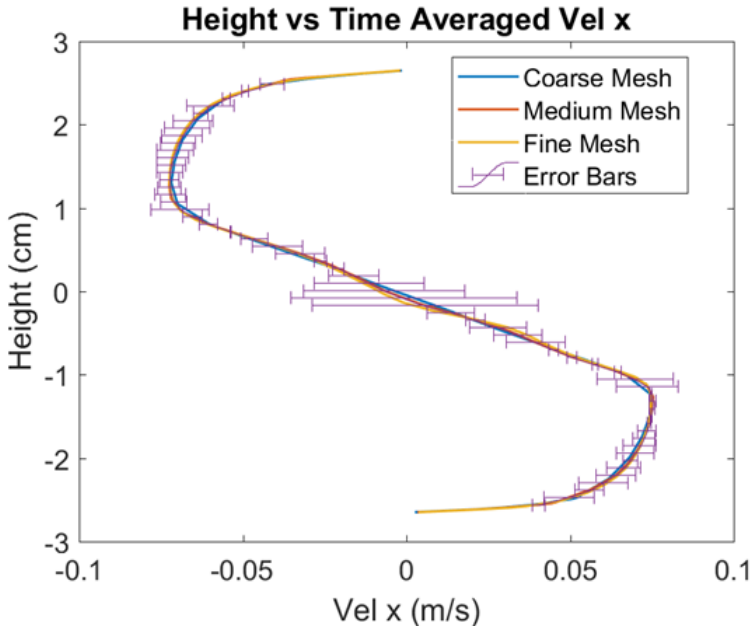

Figure 4.9: Time averaged velocity profiles of the coarse, medium and fine meshes for the time range of $6.38 - 16.38$ seconds on vertical line 1 with mesh uncertainties included

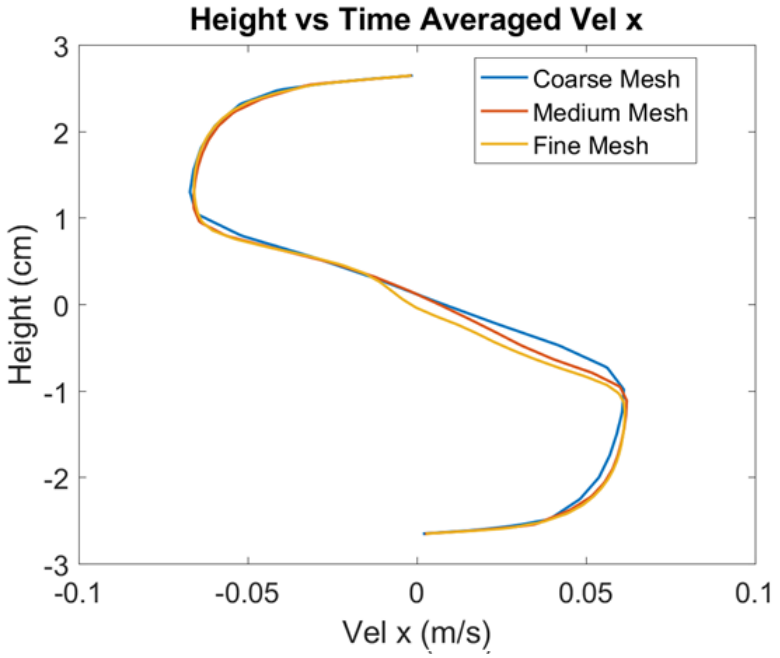

Figure 4.10: Time averaged velocity profiles of the coarse, medium and fine meshes for the time range of $16.38 - 26.38$ seconds on vertical line 1

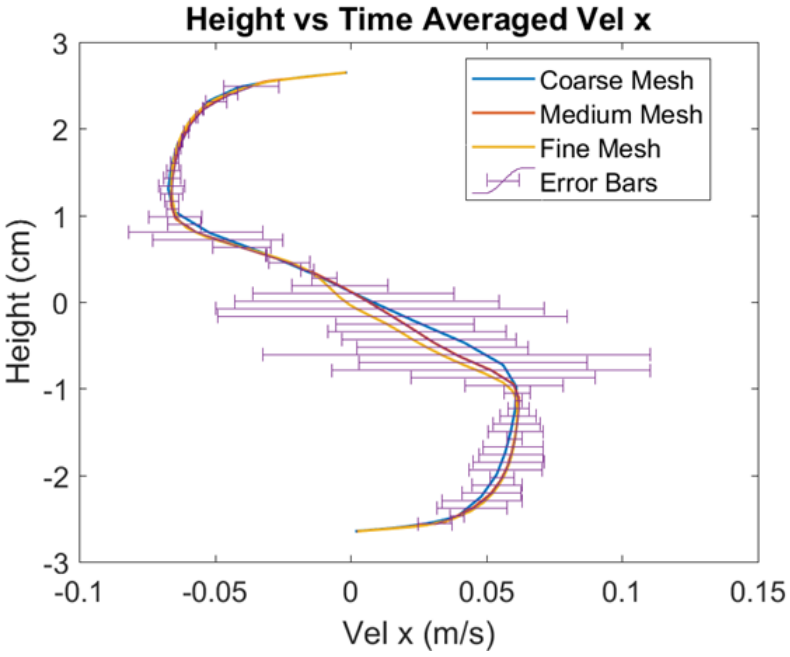

Figure 4.11: Time averaged velocity profiles of the coarse, medium and fine meshes for the time range of $16.38 - 26.38$ seconds on vertical line 1 with mesh uncertainties included

Looking at figures 4.8 through 4.21 the time-averaged values for the the x-velocity and density profiles can be seen. Due to the nature of the mathematics behind GCI and how wildly the predicted solutions vary about each other, two graphs for each quantity at each time have been provided, one with error bars and the other without. This should help the reader understand why the uncertainties, the error bars, are behaving the way they do. Looking at the errors bars, the reason the closed and strongly transient cases are so troublesome becomes evident. As time progress the bound of the error bars increase significantly. In open systems time averaging would be an option thus reducing the significance of any temporal error. A physical observance that can be made by looking at the various graphs is that the decay time of this particular flow is really long. far exceeding the 90 seconds simulated in this CFD investigation.

The difference between the coarse, medium and fine meshes are the most pronounced in the region of the pipe where the counter-current flow interface is located. It is at this region that the effects of using relatively coarse meshes, in conjunction with limited RANS models, begin to show in the results. The limited ability of the chosen physics continua to accurately resolve the appropriate density gradient, is causing the various predicted solutions to significantly deviate from each other. Compound the spatial resolution issues with the transient nature of the simulation and the limitations of the models and you get a simulation that that is difficult to extract useful data from at latter periods in time.

4.1.3 Results on Vertical Line 4

VL4, see figure 4.22 was chosen as a data probe for two reasons. Firstly, it was within the PIV window the experimentalists had chosen to measure. Secondly, it was in a region that was between the knife-valve and the nozzle leading into the downcommer region of the experiment. It was thought that these distances would isolate any potential effects that either portion of the geometry might have on the flow in this region of the cold-leg. Looking at the velocity and density profiles, presented in figures 4.23 through 4.34 and several of the same trends that were observed on the previous vertical line can be observed. Namely, the mesh uncertainties are at their largest in the interfacial portion of the cold-leg and they tend to grow with the progression of time. One notable feature at this measurement location is that the interfacial region has decreased in height. One side effect of this now reduced cross-section is that the flow velocity has increased on the lower portion of the cold-leg.

One noteworthy observation is that there are now three locations where the mesh uncertainties excessively propagate with time. The first of which, which was previously identified, was the interfacial region in the cold leg where the two fluid species meet. The second and third regions are in the area of the probe where the positive and negative components of the x-velocity are at their greatest. Take figure 4.30 for example, the three regions of greatest uncertainty are around 1.5 cm and approximately - 1.75 cm.

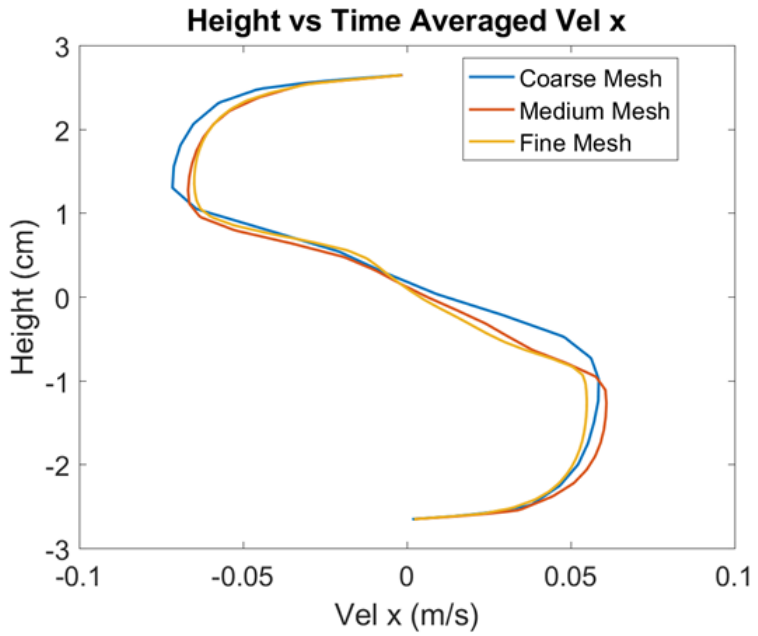

Figure 4.12: Time averaged velocity profiles of the coarse, medium and fine meshes for the time range of $25 - 35$ seconds on vertical line 1

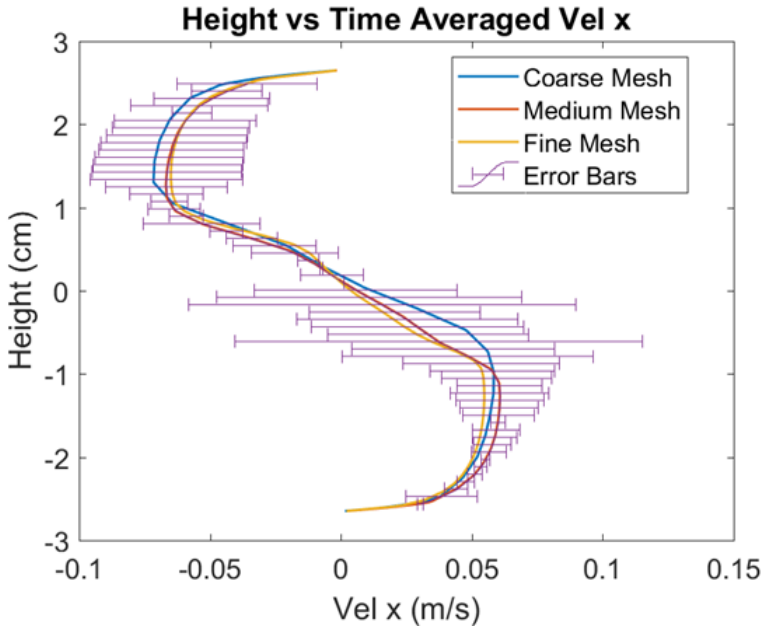

Figure 4.13: Time averaged velocity profiles of the coarse, medium and fine meshes for the time range of $25 - 35$ seconds on vertical line 1 with mesh uncertainties included

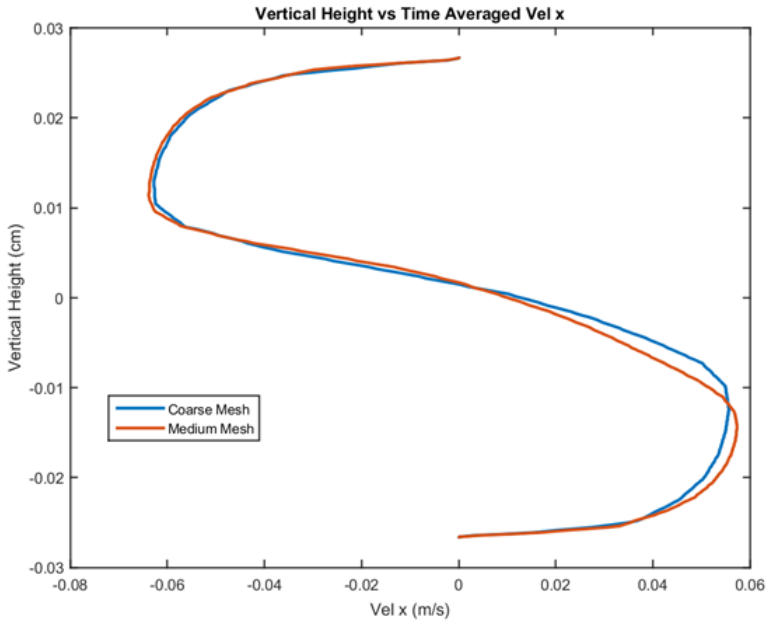

Figure 4.14: Time averaged velocity profiles of the coarse and medium meshes for the time range of $40 - 90$ seconds on vertical line 1

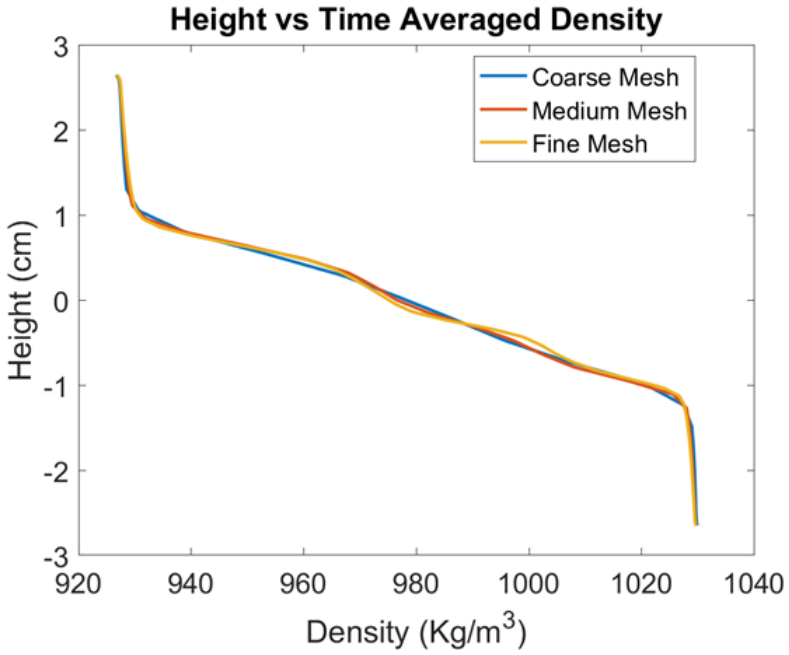

Figure 4.15: Time averaged density profiles of the coarse, medium and fine meshes for the time range of $6.38 - 16.38$ seconds on vertical line 1

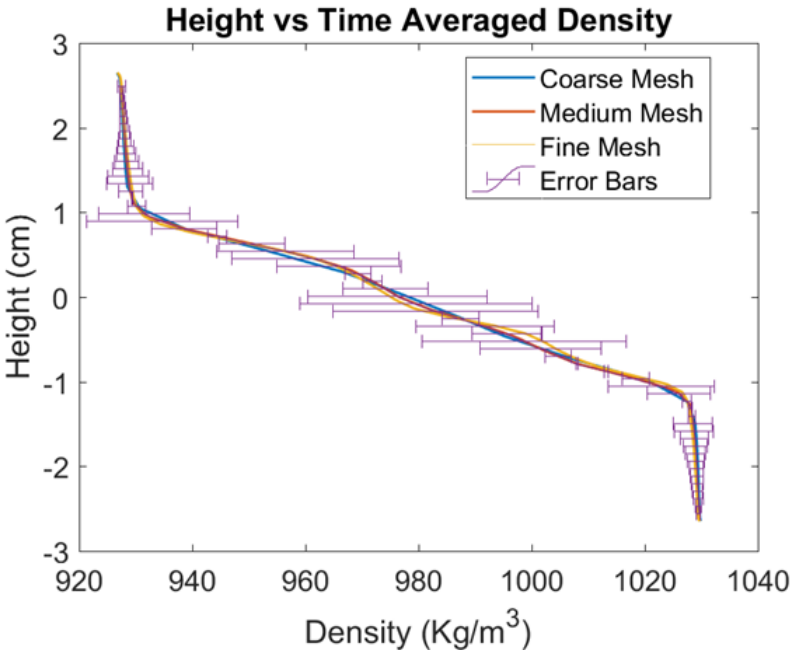

Figure 4.16: Time averaged density profiles of the coarse, medium and fine meshes for the time range of $6.38 - 16.38$ seconds on vertical line 1 with mesh uncertainties included

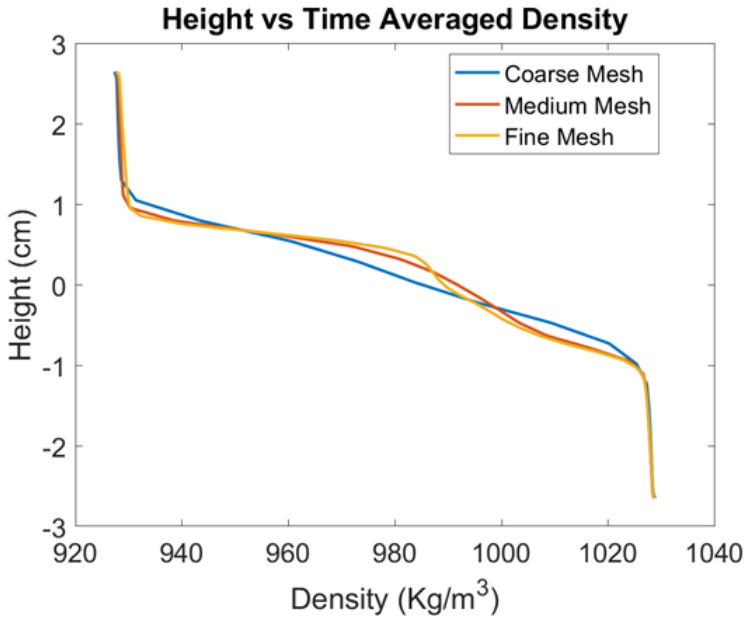

Figure 4.17: Time averaged density profiles of the coarse, medium and fine meshes for the time range of $16.38 - 26.38$ seconds on vertical line 1

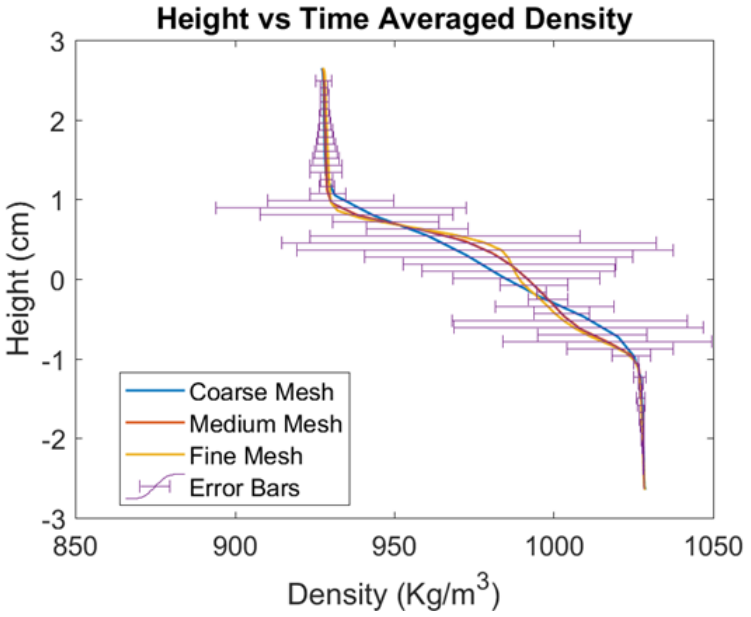

Figure 4.18: Time averaged density profiles of the coarse, medium and fine meshes for the time range of $16.38 - 26.38$ seconds on vertical line 1 with mesh uncertainties included

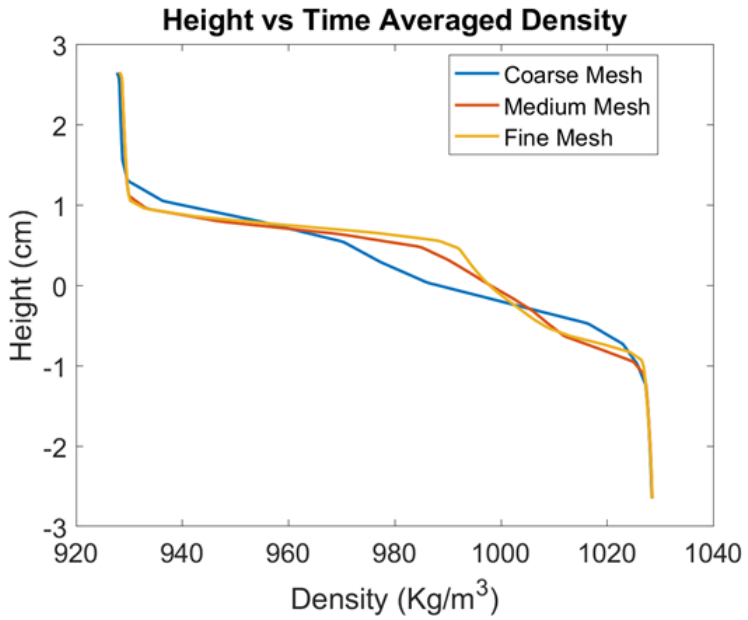

Figure 4.19: Time averaged density profiles of the coarse, medium and fine meshes for the time range of $25 - 35$ seconds on vertical line 1

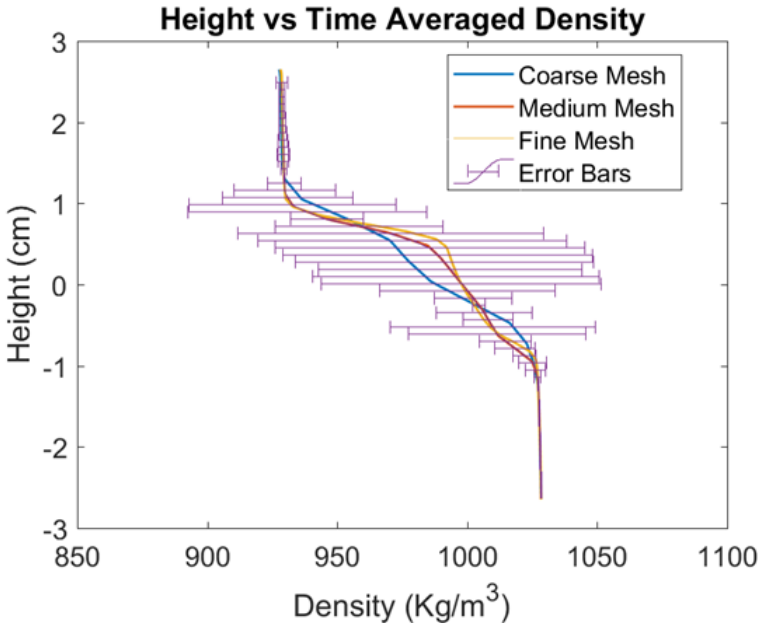

Figure 4.20: Time averaged density profiles of the coarse, medium and fine meshes for the time range of $25 - 35$ seconds on vertical line 1 with mesh uncertainties included

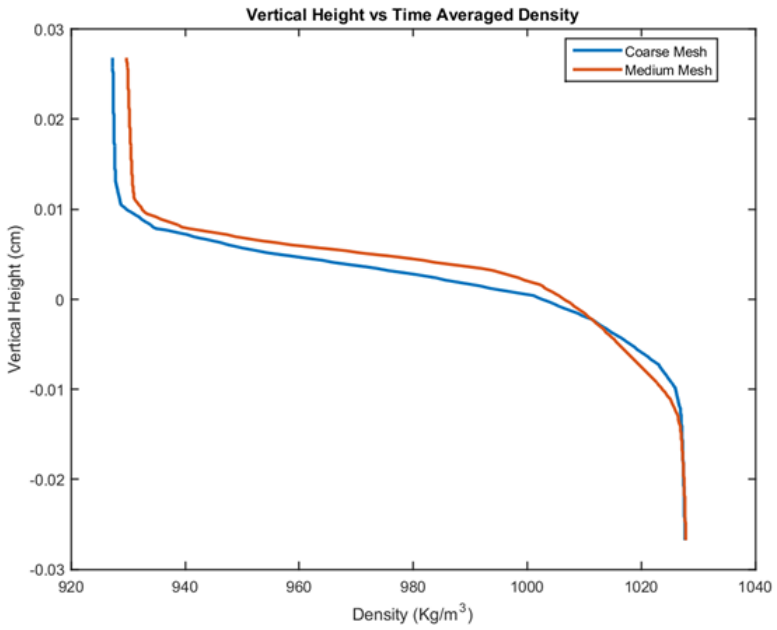

Figure 4.21: Time averaged density profiles of the coarse and medium meshes for the time range of $45 - 90$ seconds on vertical line 1

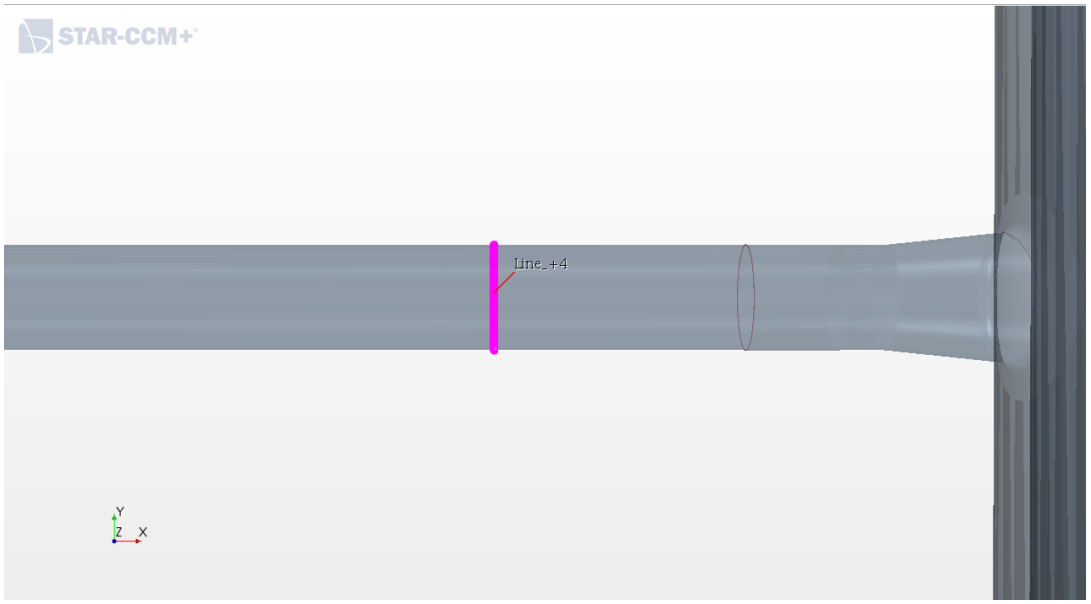

Figure 4.22: Visualization of Vertical Line 4. This line is located close to the initial knife valve separating the domain.

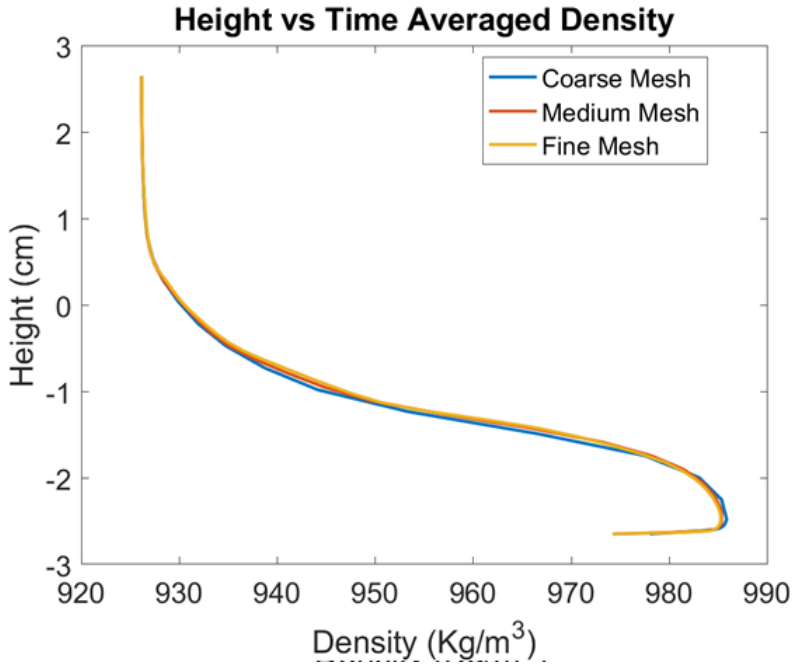

Figure 4.23: Time averaged density profiles of the coarse, medium and fine meshes for the time range of $6.38 - 16.38$ seconds on vertical line 4

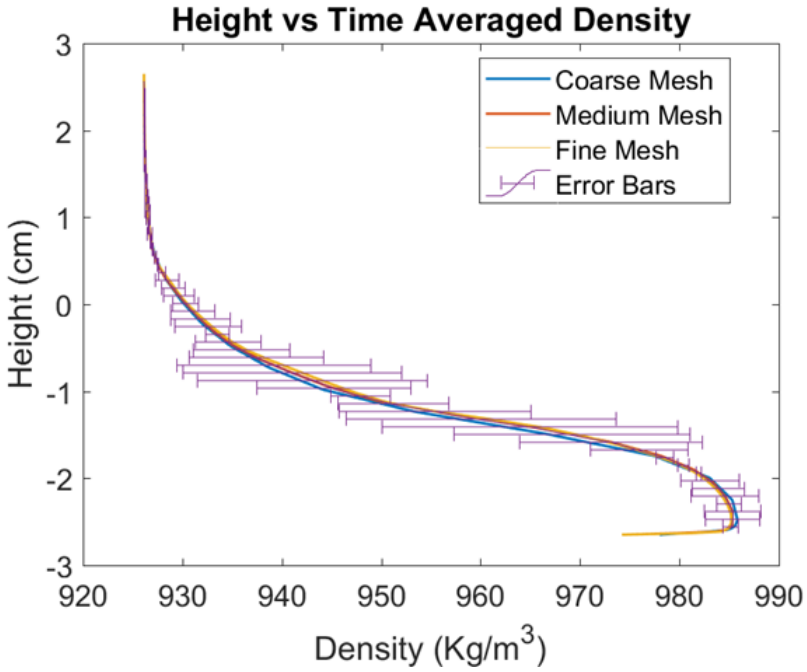

Figure 4.24: Time averaged density profiles of the coarse, medium and fine meshes for the time range of $6.38 - 16.38$ seconds on vertical line 4 with mesh uncertainties included

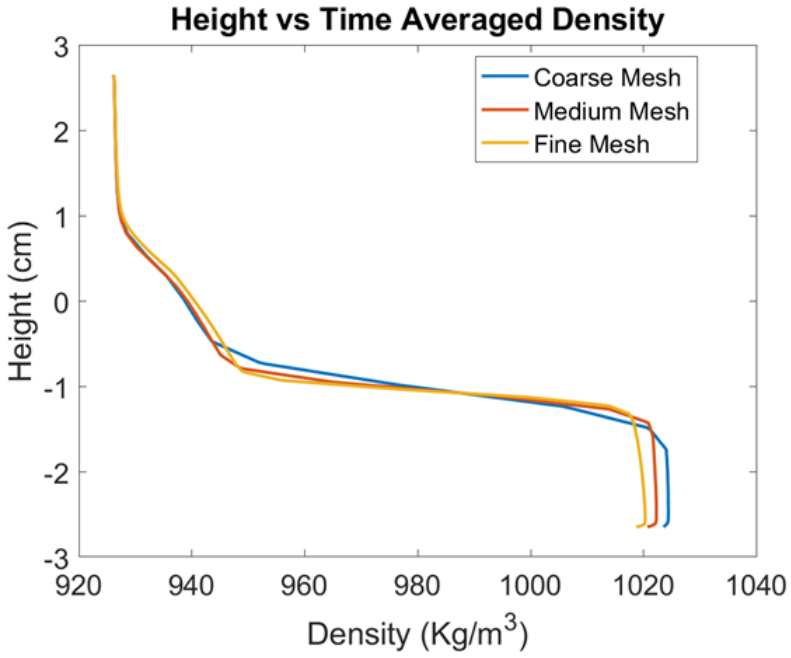

Figure 4.25: Time averaged density profiles of the coarse, medium and fine meshes for the time range of $16.38 - 26.38$ seconds on vertical line 4

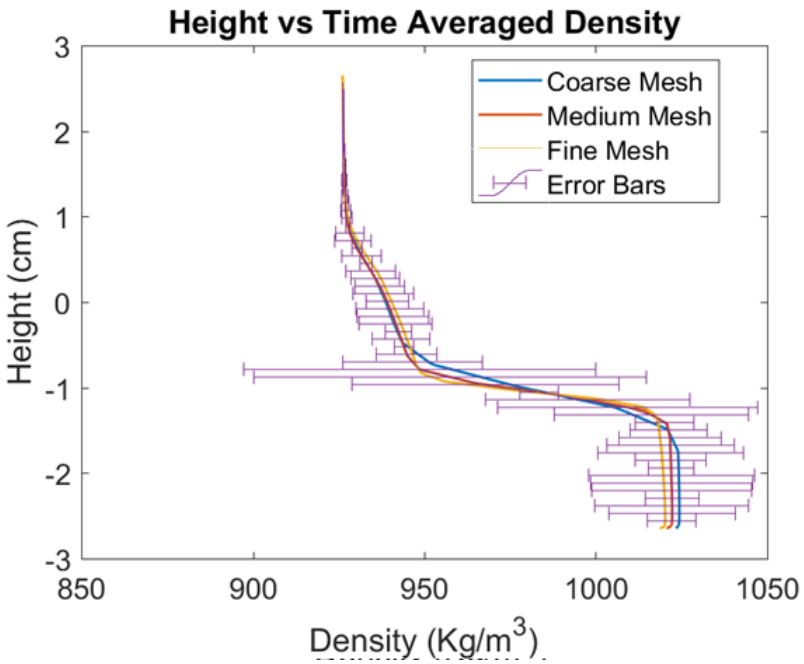

Figure 4.26: Time averaged density profiles of the coarse, medium and fine meshes for the time range of $16.38 - 26.38$ seconds on vertical line 4 with mesh uncertainties included

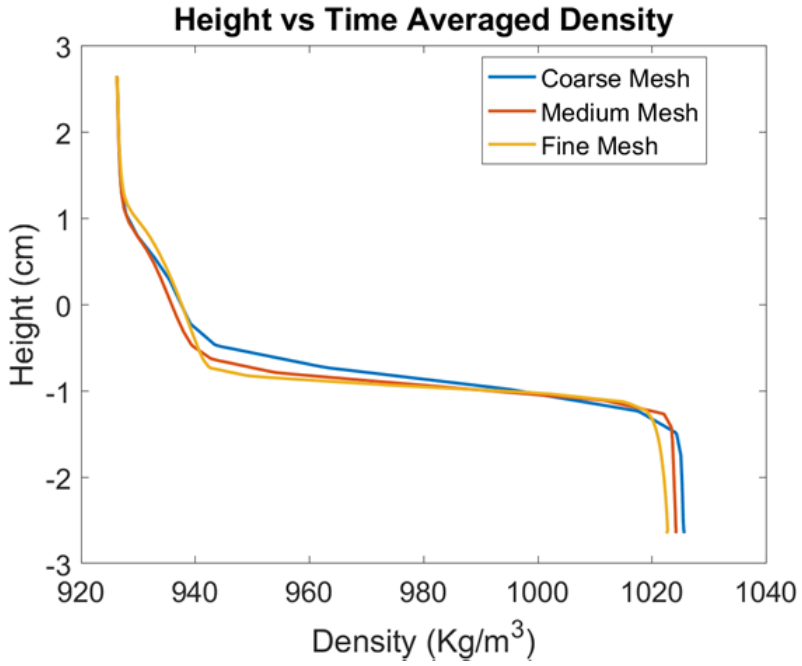

Figure 4.27: Time averaged density profiles of the coarse, medium and fine meshes for the time range of $25 - 35$ seconds on vertical line 4

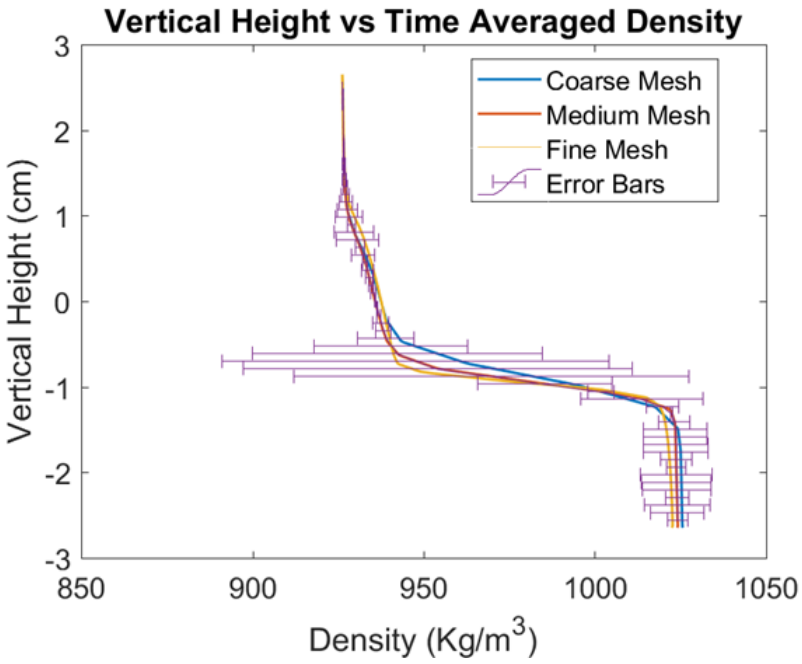

Figure 4.28: Time averaged density profiles of the coarse, medium and fine meshes for the time range of $25 - 35$ seconds on vertical line 4 with mesh uncertainties included

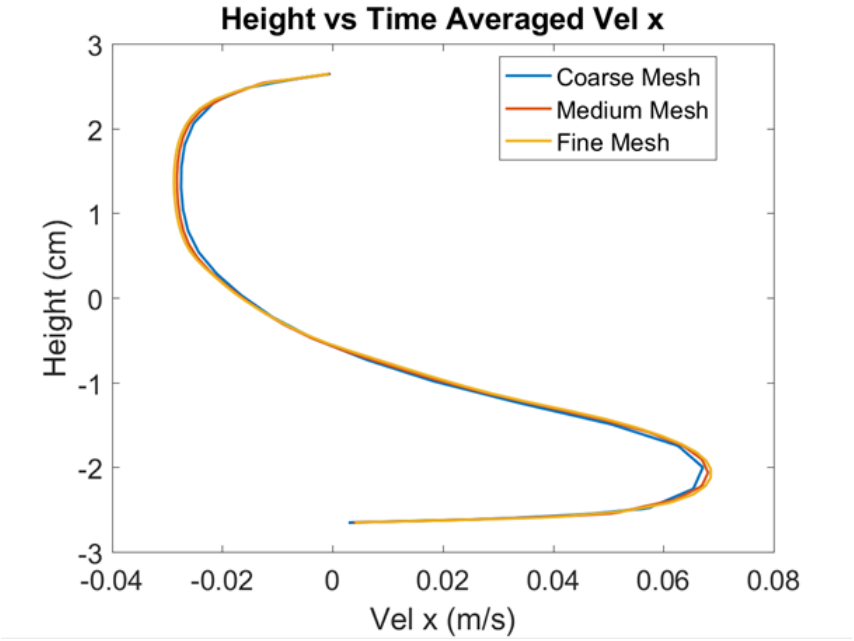

Figure 4.29: Time averaged density profiles of the coarse, medium and fine meshes for the time range of $6.38 - 16.38$ seconds on vertical line 4

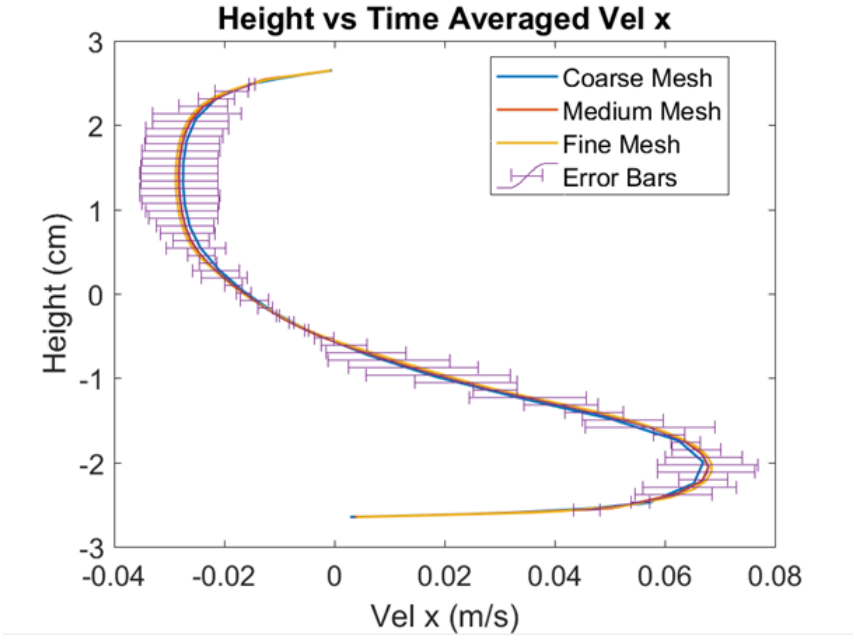

Figure 4.30: Time averaged density profiles of the coarse, medium and fine meshes for the time range of $6.38 - 16.38$ seconds on vertical line 4 with mesh uncertainties included

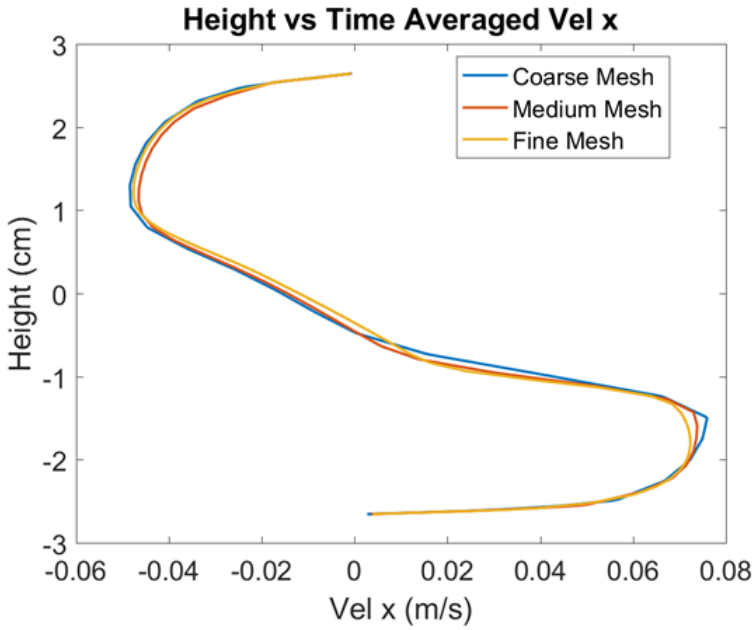

Figure 4.31: Time averaged density profiles of the coarse, medium and fine meshes for the time range of $16.38 - 26.38$ seconds on vertical line 4

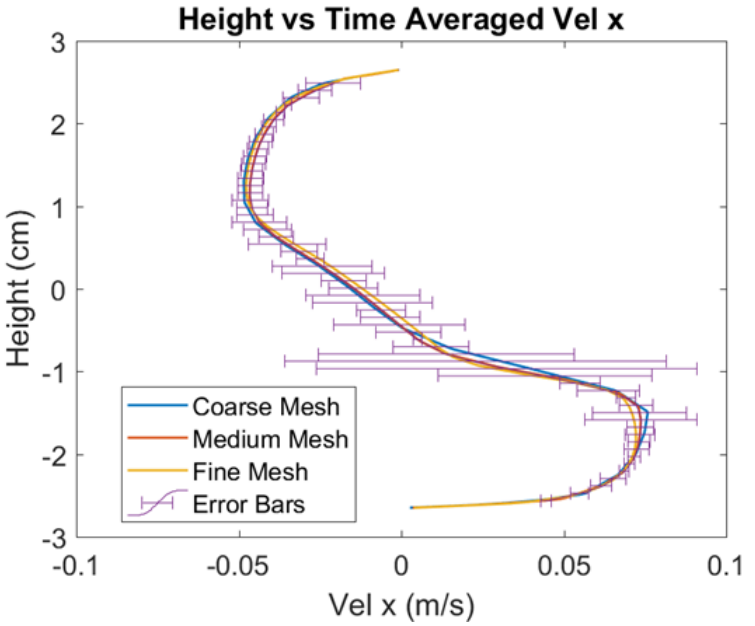

Figure 4.32: Time averaged density profiles of the coarse, medium and fine meshes for the time range of $16.38 - 26.38$ seconds on vertical line 4 with mesh uncertainties included

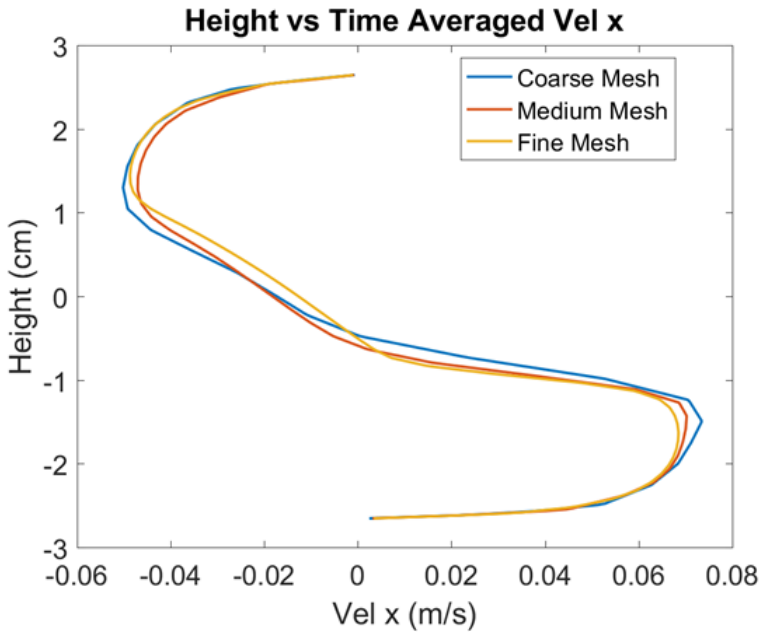

Figure 4.33: Time averaged density profiles of the coarse, medium and fine meshes for the time range of $25 - 35$ seconds on vertical line 4

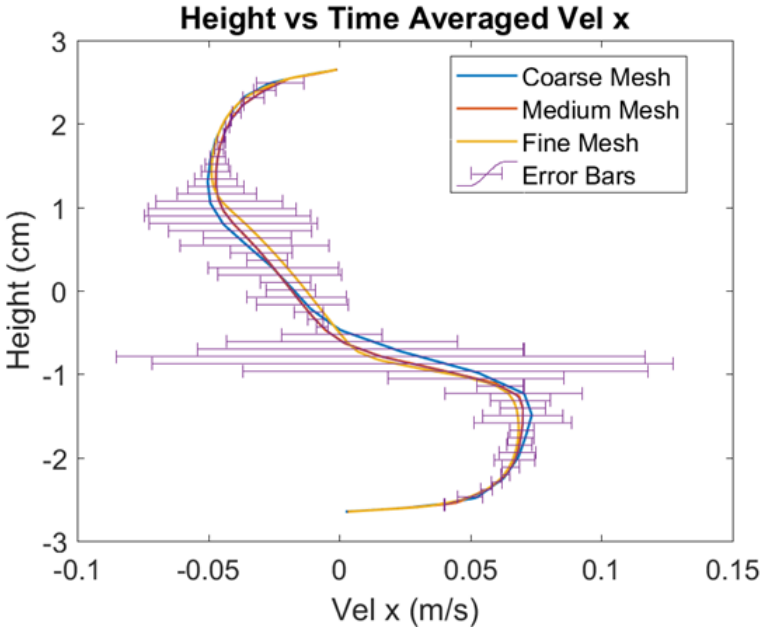

Figure 4.34: Time averaged density profiles of the coarse, medium and fine meshes for the time range of $25 - 35$ seconds on vertical line 4 with mesh uncertainties included

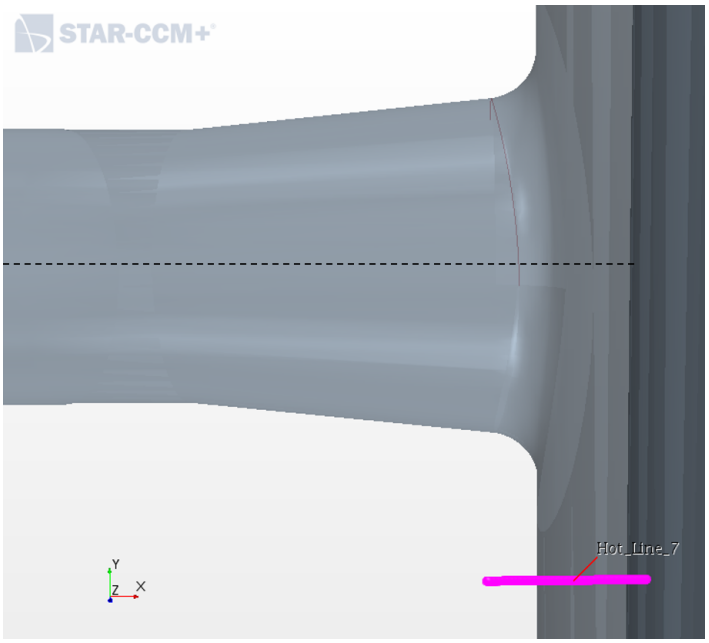

Figure 4.35: Visualization of Horizontal Line 7. This line is located close to the initial knife valve separating the domain.

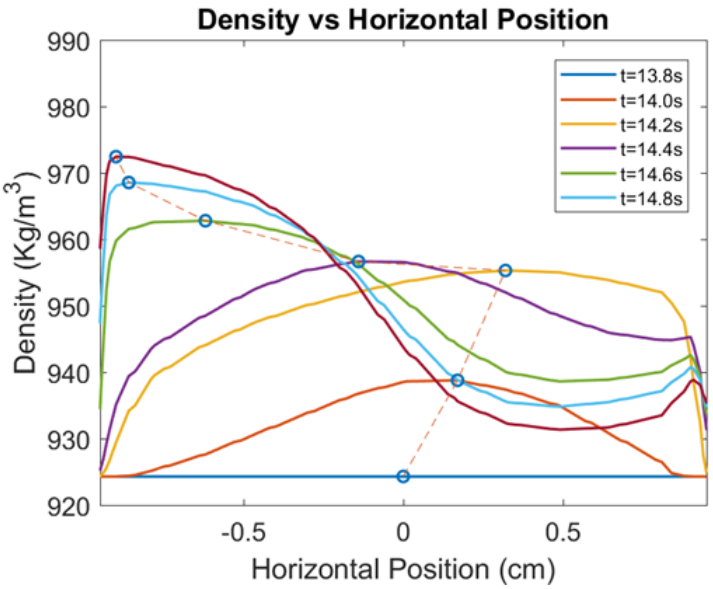

Figure 4.36: The developmental density profiles on horizontal line 7

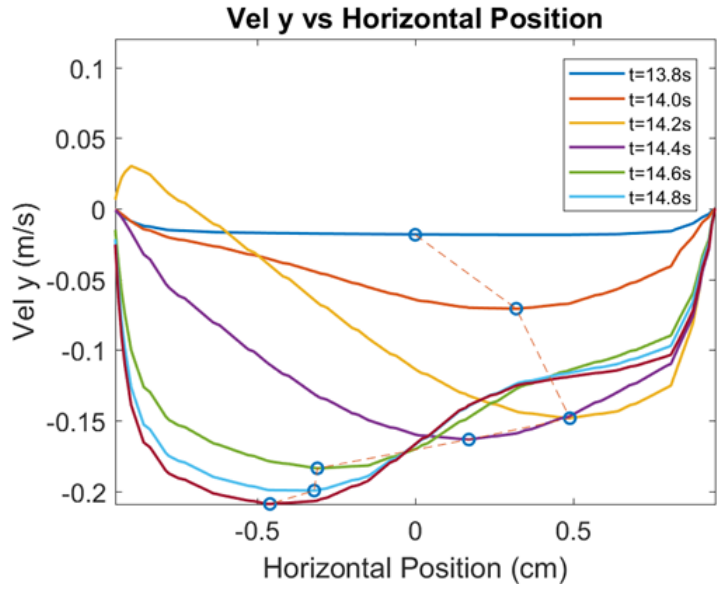

Figure 4.37: The developmental velocity profiles on horizontal line 7

4.1.4 Results on Horizontal Line 7

HL7 is the first horizontal measurement in the downcommer region, it is the closest line probe to the EDF nozzle. The logic behind the selection of this probe location was that by having it so close to the nozzle it would be easy to determine the severity of any potential flow separation. Since the goal of the experiment was to characterize the degree of mixing in this portion of the geometry, it made sense to ensure a probe location captured the fluid fronts entrance into this portion of the domain. Looking at figures 4.36 & 4.37 a similar set of developmental velocity and density profiles are presented. The development of the flow as it crests the nozzle takes nearly twice as long as the flow profile in the cold-leg. Initially the fluid front separates from the nozzle, as indicated by the maximum density and velocity locations, and after about a second they quickly reattach to the pressure vessel wall. It should be noted that the yellow line on figure 4.37, which represents a time of 14.2 seconds, shows a positive y-velocity. It is speculated that as the jet crests the nozzle, bouyancy effects suspend the front for a moment thus allowing it to separate. Once the lighter fluid is displaced the low velocity front reattached to the wall.

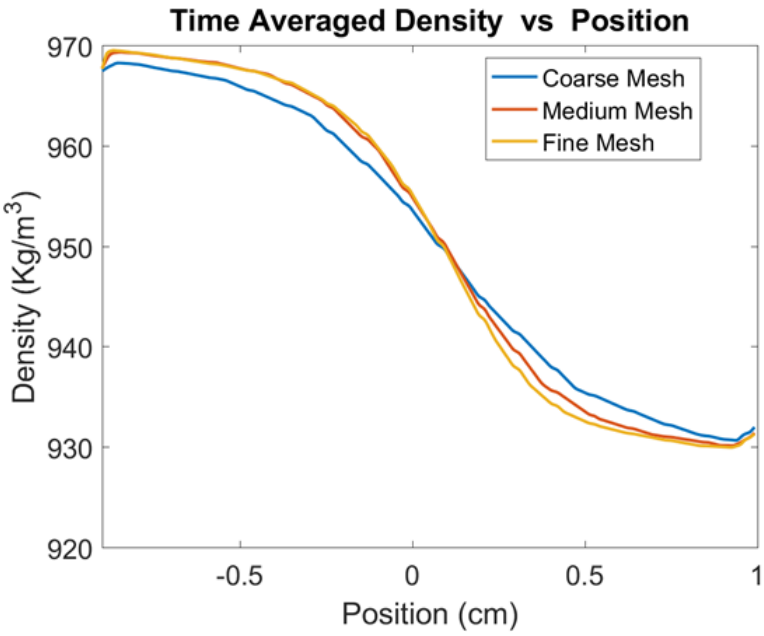

Figure 4.38: Time averaged density profiles of the coarse, medium and fine meshes for the time range of $10.84 - 20.84$ seconds on horizontal line 7

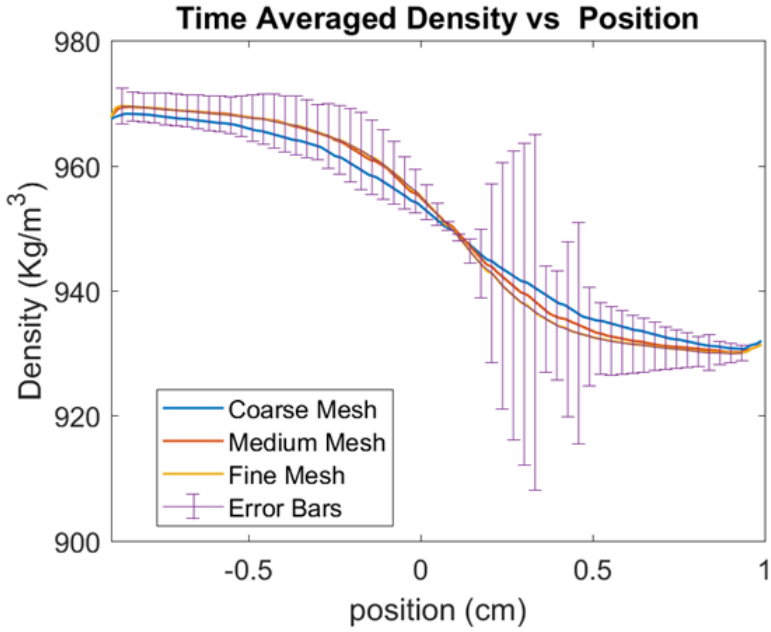

Figure 4.39: Time averaged density profiles of the coarse, medium and fine meshes for the time range of $10.84 - 20.84$ seconds on horizontal line 7 with mesh uncertainties included

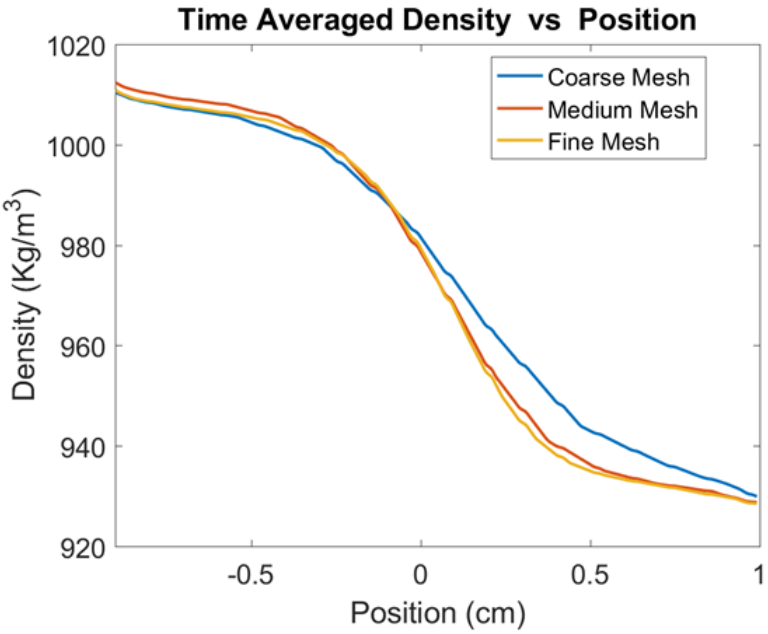

Figure 4.40: Time averaged density profiles of the coarse, medium and fine meshes for the time range of $20.84 - 30.84$ seconds on horizontal line 7

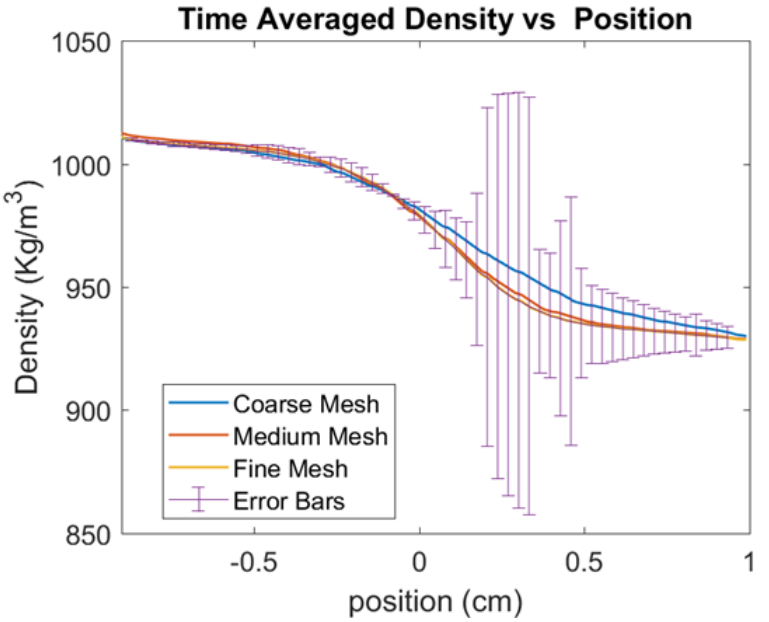

Figure 4.41: Time averaged density profiles of the coarse, medium and fine meshes for the time range of $20.84 - 30.84$ seconds on horizontal line 7 with mesh uncertainties included

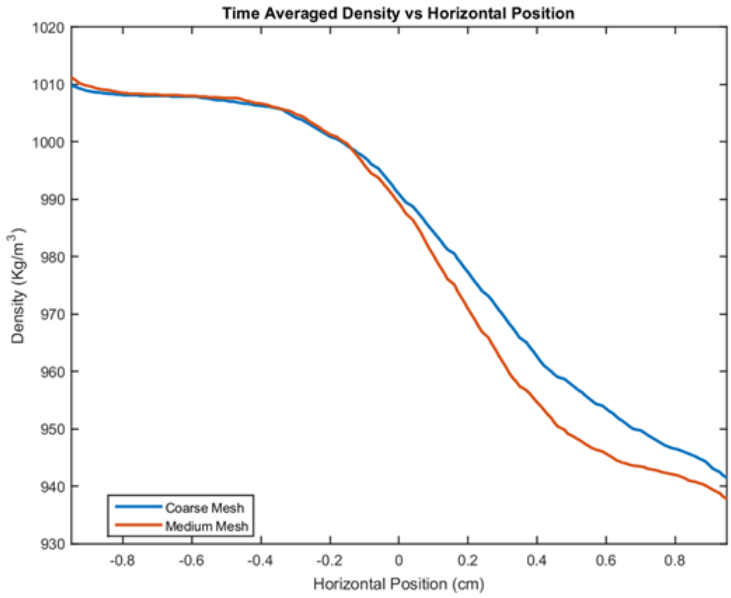

Figure 4.42: Time averaged density profiles of the coarse and medium meshes for the time range of $45 - 90$ seconds on horizontal line 4

Looking at figures 4.38 through 4.47 a lot of the trends that existed in the cold-leg exist in the downcommer as well. There is one major difference however, the disparities in the values of both velocity and density are more profound across the three meshes. It is speculated that because it takes nearly 14 seconds for the front to even reach this point in the domain, and small differences between the mesh get accentuated over the long time period. As previously mentioned, since this is a closed system the difficulty of generating relevant temporal measurements is exceeding large. To highlight this point one needs only to look at the time averaging window of each set of figures. While they seem like they were specifically chosen, they were, it wasn't for any reason pertaining to the geometry or flow physics. In fact the selection of the time window was done solely based on the availability of experimental data.

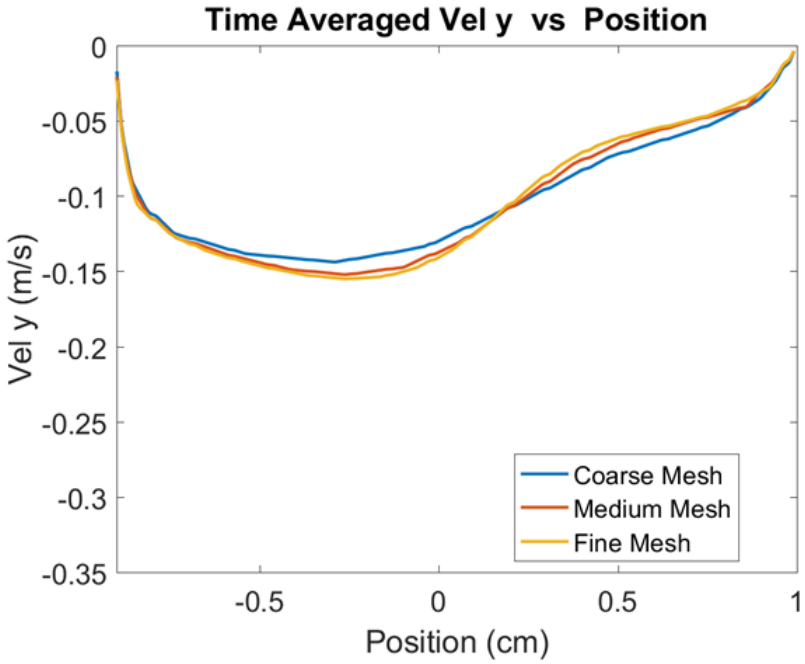

Figure 4.43: Time averaged velocity profiles of the coarse, medium and fine meshes for the time range of $10.84 - 20.84$ seconds on horizontal line 7

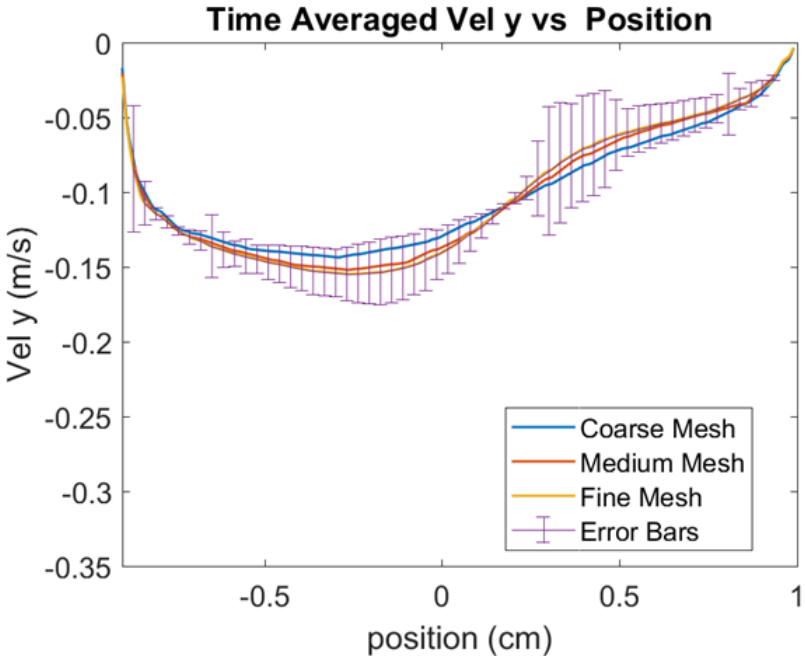

Figure 4.44: Time averaged velocity profiles of the coarse, medium and fine meshes for the time range of $10.84 - 20.84$ seconds on horizontal line 7 with mesh uncertainties included

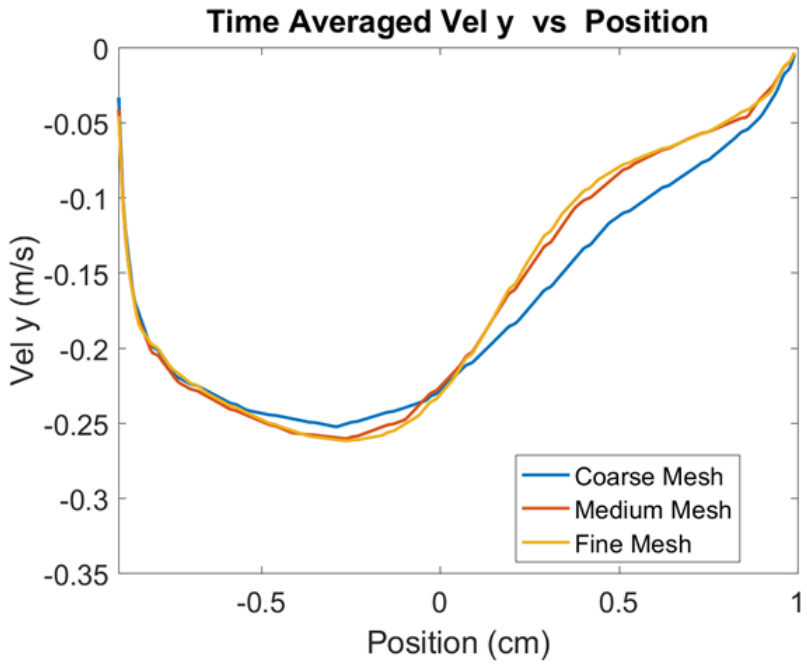

Figure 4.45: Time averaged velocity profiles of the coarse, medium and fine meshes for the time range of $20.84 - 30.84$ seconds on horizontal line 7

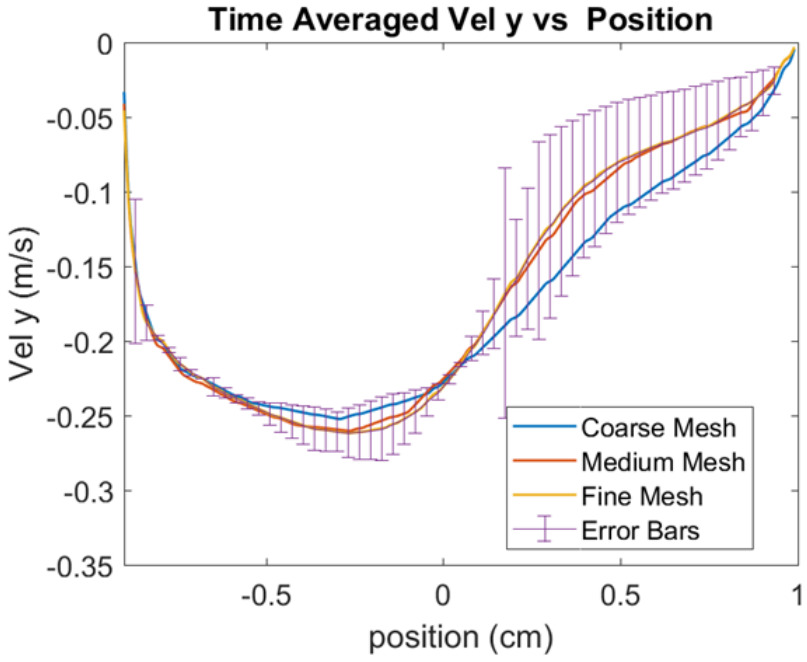

Figure 4.46: Time averaged velocity profiles of the coarse, medium and fine meshes for the time range of $20.84 - 30.84$ seconds on horizontal line 7 with mesh uncertainties included

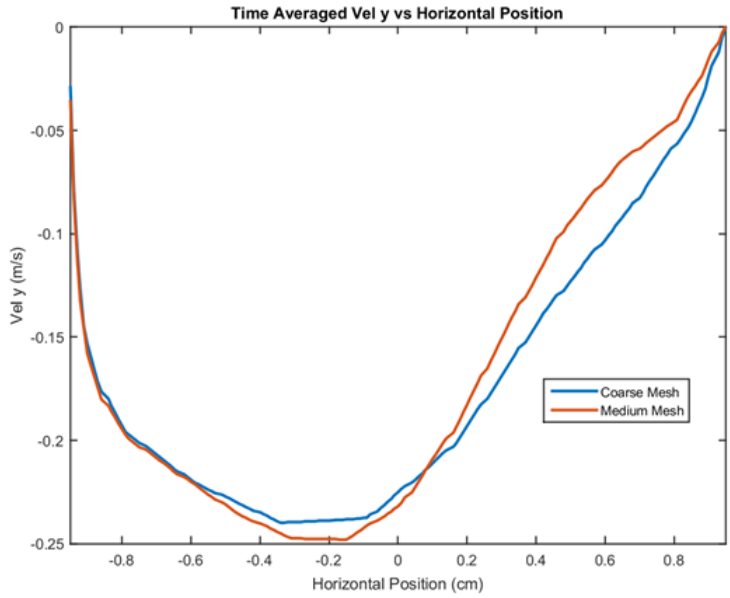

Figure 4.47: Time averaged density profiles of the coarse and medium meshes for the time range of $45 - 90$ seconds on horizontal line 7

4.1.5 Results on Horizontal Line 12

The first downcommer probe, HL7, was selected because of its relevance, due to its proximity to the EDF nozzle, to the overall state of the flow in this portion of the domain. Keeping with the pattern HL12 was selected simply because it lied in the experimental PIV window. Looking at figures 4.49 through 4.52 it is clearly seen where the mesh uncertainties are the greatest. Again, given how long it takes for the fluid front to reach this location in the domain, it is speculated the minute differences in the solution, at earlier times, are the cause of the disparities bewtween the meshes.Strangely enough the uncertainties of the y-velocity field have, relatively, settled down. This is attributed to the significant increase in the turbulence in this region of the downcommer. This is visually corroborated by figures 4.53 through 4.56, though it should be noted that there are some atypically large uncertainties near the walls of the downcommer region.

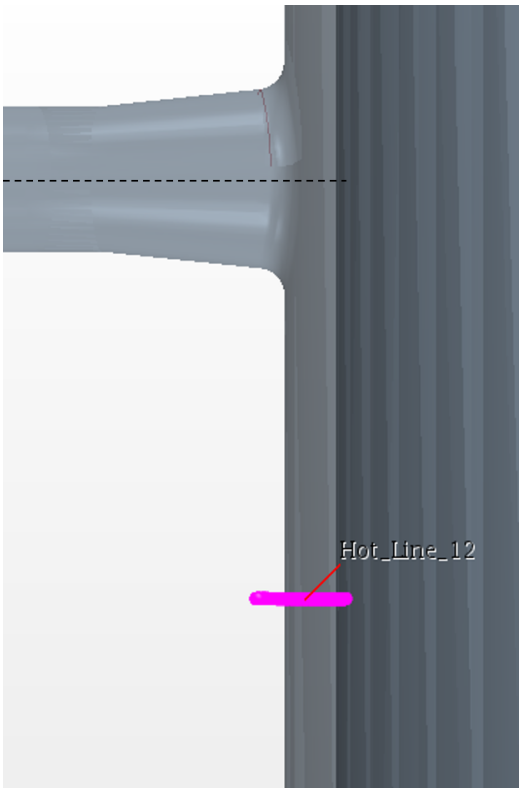

Figure 4.48: Visualization of Horizontal Line 12. This line is located close to the initial knife valve separating the domain.

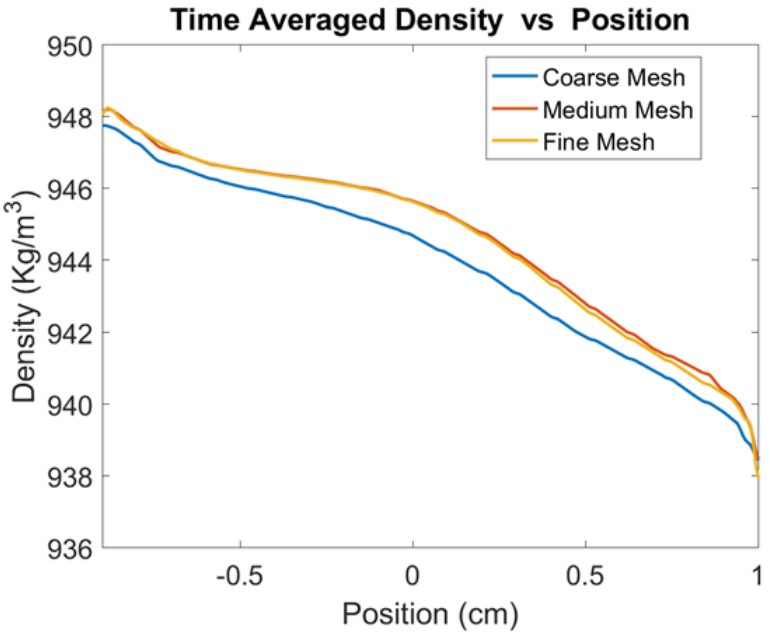

Figure 4.49: Time averaged density profiles of the coarse, medium and fine meshes for the time range of $10.84 - 20.84$ seconds on horizontal line 12

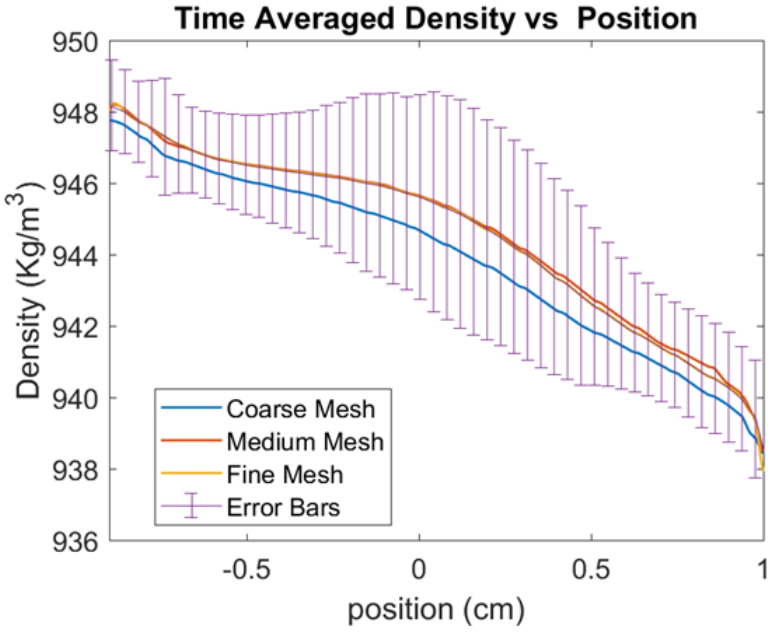

Figure 4.50: Time averaged density profiles of the coarse, medium and fine meshes for the time range of $10.84 - 20.84$ seconds on horizontal line 12 with mesh uncertainties included

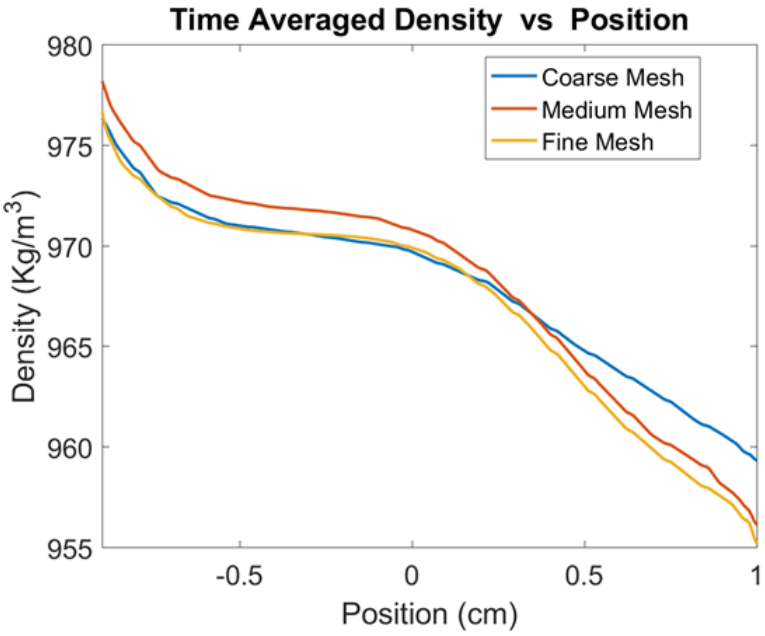

Figure 4.51: Time averaged density profiles of the coarse, medium and fine meshes for the time range of $20.84 - 30.84$ seconds on horizontal line 12

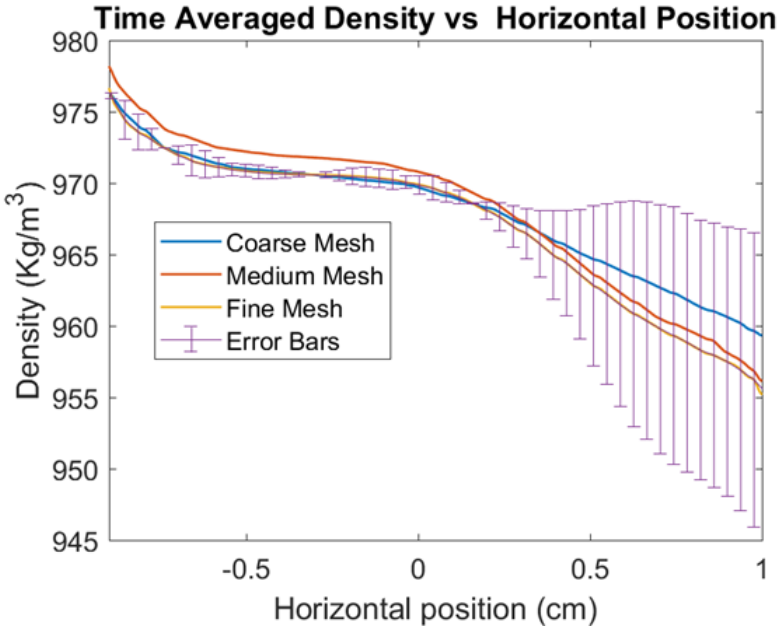

Figure 4.52: Time averaged density profiles of the coarse, medium and fine meshes for the time range of $20.84 - 30.84$ seconds on horizontal line 12 with mesh uncertainties included

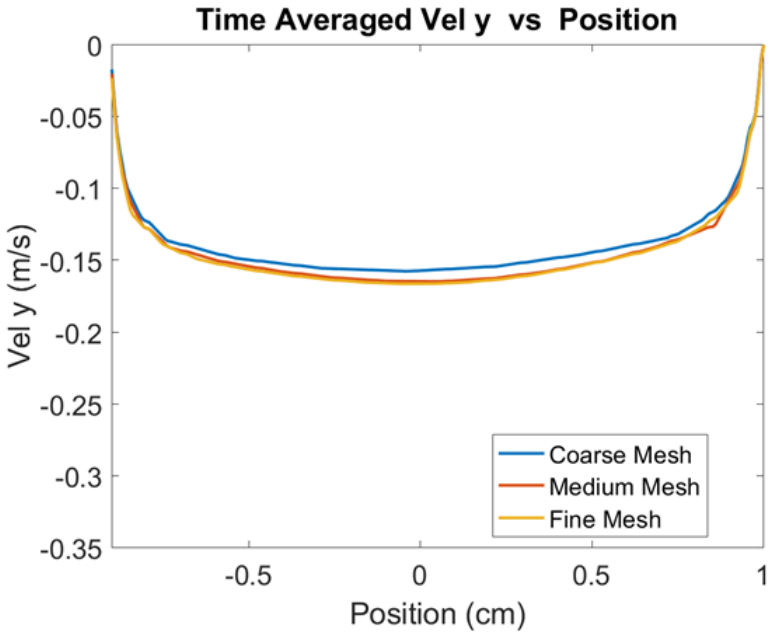

Figure 4.53: Time averaged velocity profiles of the coarse, medium and fine meshes for the time range of $10.84 - 20.84$ seconds on horizontal line 12

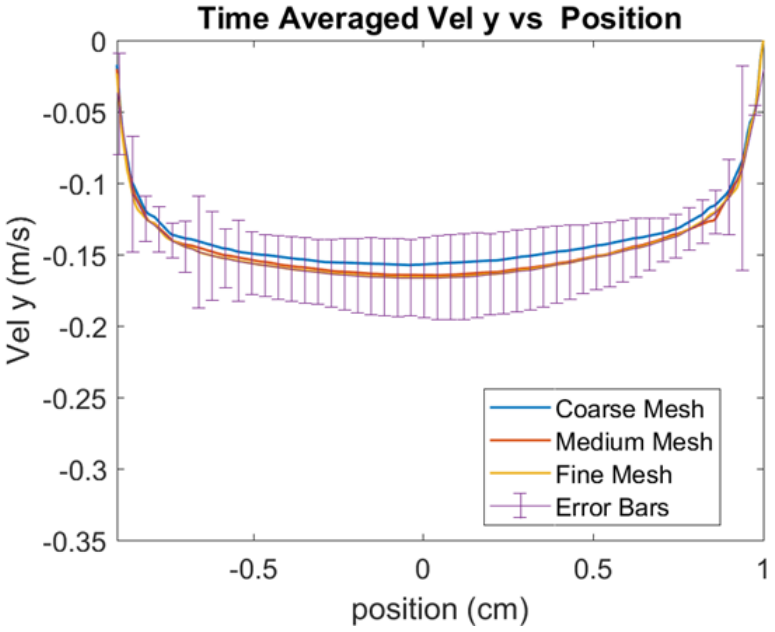

Figure 4.54: Time averaged velocity profiles of the coarse, medium and fine meshes for the time range of $10.84 - 20.84$ seconds on horizontal line 12 with mesh uncertainties included

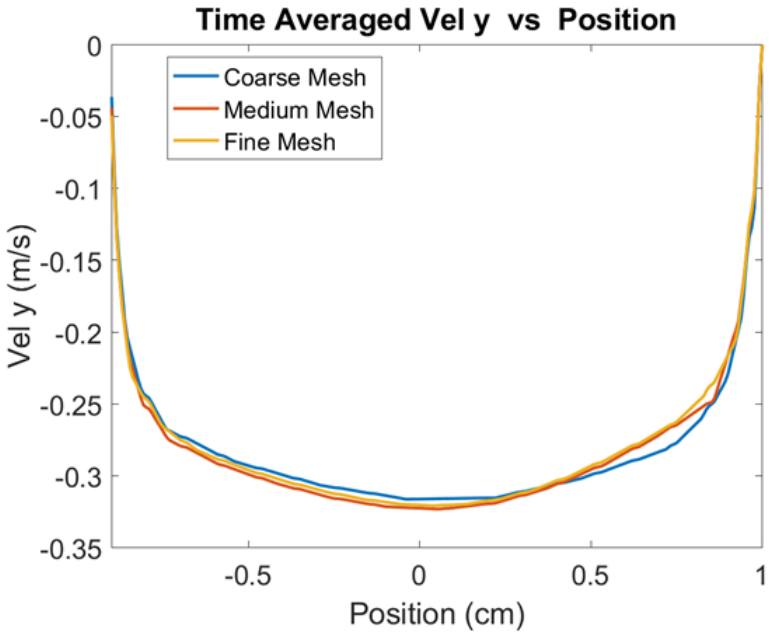

Figure 4.55: Time averaged velocity profiles of the coarse, medium and fine meshes for the time range of $20.84 - 30.84$ seconds on horizontal line 12

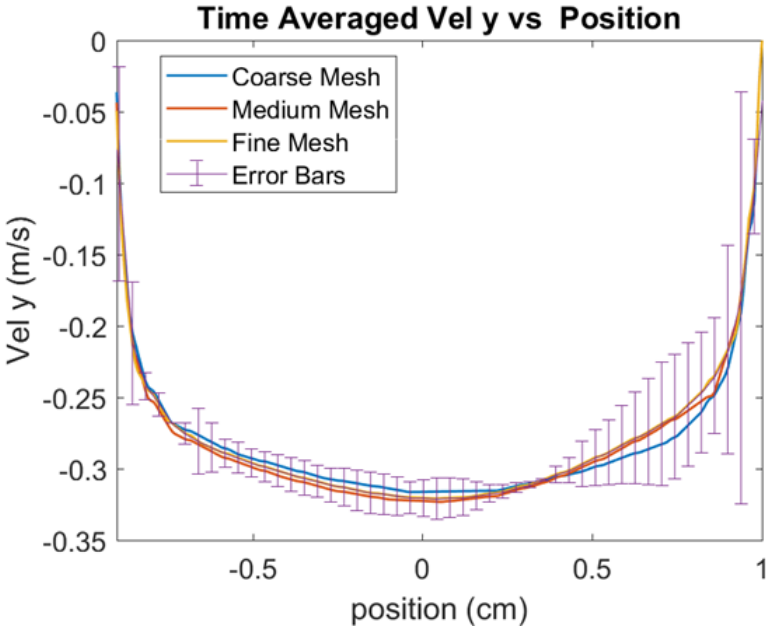

Figure 4.56: Time averaged velocity profiles of the coarse, medium and fine meshes for the time range of $20.84 - 30.84$ seconds on horizontal line 12 with mesh uncertainties included

4.1.6 Preliminary Experimental Comparisons

Prior to making comparison between the experimental data and the preliminary simulations it should be noted that the two analyses utilized varying material properties. Tables 4.1 - 4.3 are better able to highlight the difference between the two cases. With that in mind, looking at figures 4.57 and 4.58 a couple observations can be made. Most obvious is the significant difference in the velocity profiles, nearly 125% for the first 10 second time window and almost 100% for the second ten second frame. This difference is primarily attributed to the experiment having a roughly, 3.7% larger density difference between the two cases and a nearly 4% increased viscosity. That being said, the profiles, and the location of the interfacial region in the cold leg match up decently.

More information, however, is able to be gleaned from the comparison of experimental data and the predicted profiles on HL12. Starting with figure 4.59 three facts become readily evident. Firstly, the data provided by the experimentalists is nowhere near as homogenized as the simulated data. Secondly there is a clear bias towards the reactor vessel wall indicating that there is not only flow separation from the exterior wall but it is consistent in time. The third fact is a mere observation, which was touched upon in the analysis of the cold-leg velocity profiles, but it should be noted that the peak velocity profile from the data set is nearly 100% greater than the peak velocity in the simulation.

Looking at figure 4.60 the predicted velocity profile interestingly exceeds, though not by the same margins, the experimental data set. While disparities in data sets like this are not desired in final production runs, they are useful in helping highlight potential challenges in a particular problem prior to the commitment of large scale resources. In this instance it is speculated that the difference in the y-velocity component values are due primarily to temporal causes. To summarize, the farther away from the initial condition the simulations get, the more the predicted solutions diverge from not only the experimental data, but themselves as well.

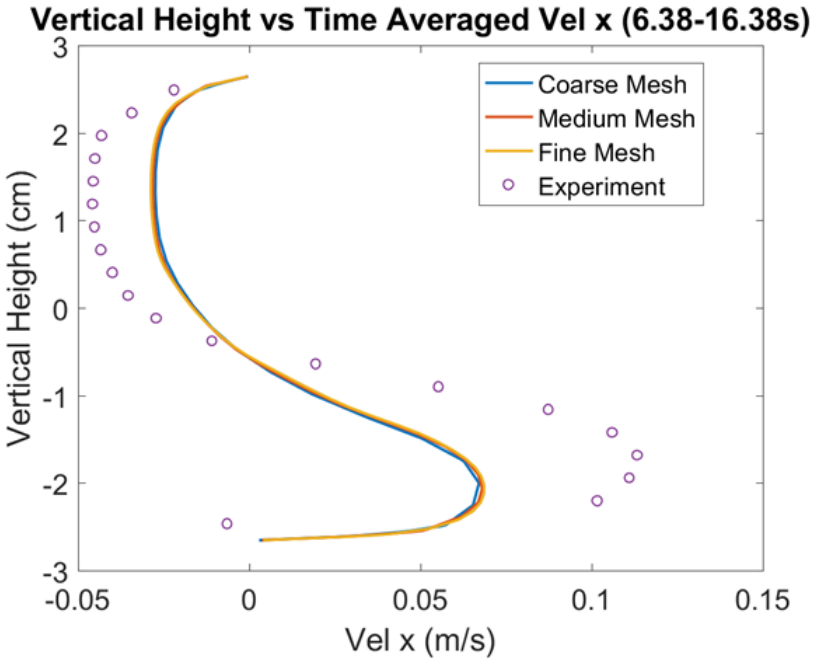

Figure 4.57: Experimental data x-velocity data compared against the simulated, Time averaged velocity profiles of the coarse, medium and fine meshes for the time range of $6.38 - 16.38$ seconds on vertical line 4

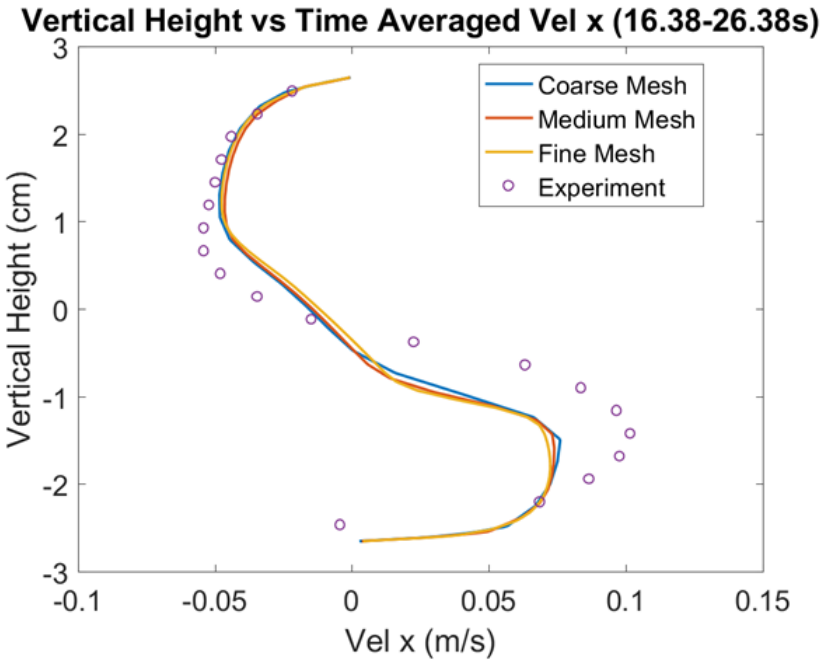

Figure 4.58: Experimental data x-velocity data compared against the simulated, Time averaged velocity profiles of the coarse, medium and fine meshes for the time range of $6.38 - 16.38$ seconds on vertical line 4

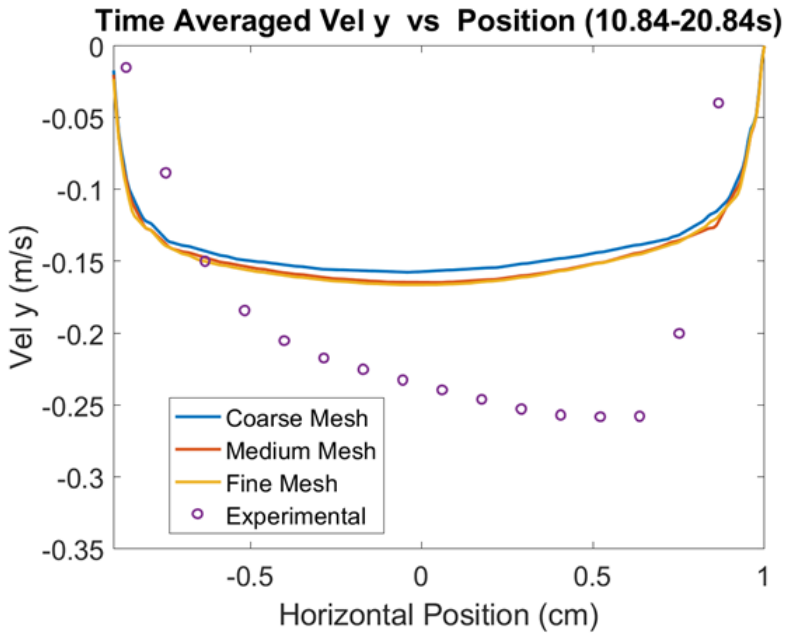

Figure 4.59: Experimental data y-velocity data compared against the simulated, Time averaged velocity profiles of the coarse, medium and fine meshes for the time range of $10.84 - 20.84$ seconds on horizontal line 12

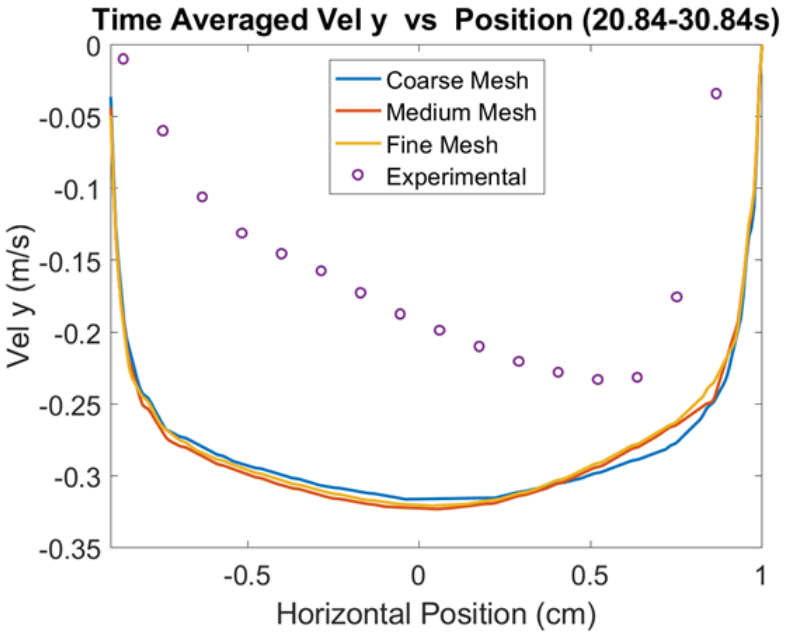

Figure 4.60: Experimental data y-velocity data compared against the simulated, Time averaged velocity profiles of the coarse, medium and fine meshes for the time range of $20.84 - 30.84$ seconds on horizontal line 12

5. SUMMARY AND CONCLUSIONS

5.1 Conclusion

The CSNI is interested on characterizing the severity of mixing in the downcommer region of a prototypical reactor geometry. To this end a series of preliminary simulations were conducted in order to guide the experimental collection of data in support of the 5th V&V benchmark on the topic. While not the subject of this thesis or the V&V benchmark, these cold-leg mixing experimental analyses have their roots grounded in work related to pressurized thermal shock. Scoping runs were set up utilizing Star CCM+, developed by Siemen's. The experimental geometry was created by the experimental group in Solid Works at TAMU and the fluid volume was extracted and refined in accordance with the prescribed assumptions. The Standard k-epsilon model was used due it already having buoyancy terms integrated into its turbulence model terms. The two-layer formulation was also applied in order to provide the model with a modicum of robustness as it was not know for sure what flow velocities and regimes would be seen in each portion of the domain. Preliminary comparisons with data derived from the experimental analysis also provided many ways in which the simulations can be improved upon to better reflect the reality observed in the experiment.

1. Investigate the potential impact of hybrid modeling techniques.

2. Investigate the impact that fully structured meshing has on the efficacy of the simulated results

3. Apply more accurate material properties and definitions for the turbulent and molecular Schmidt numbers

On the first topic, the application of hybrid models such as Detached Eddy Simulations or Partially Averaged Navier-Stokes Equations might assist in the realization of more accurate results. In the cold-leg the flow was orderly, slow moving and likely laminar. With the exception of the interfacial region it is likely this is the case in the entirety of the transfer pipe, however, future studies need to gather data on the local Reynolds number in order to asses the validity of this claim.

Now the geometry is set and is not soon to be subject to any major changes, the benefits of unstructured meshing are not worth the price their easy construction tolls. The benefits in speed and computational efficiency far outweigh the cost associated with having to tailor a mesh by hand for this particular geometry. The next generation of cold-leg mixing meshes are currently being generated in preparation for the V&V study. Similar to how the geometry was once being rapidly iterated upon, so too were the material properties. Now that the experimental fluids have been locked down and measurement techniques developed, attempting to make relevant comparisons with CFD is now viable. Future work includes concluding the three aforementioned concluding remarks in a simulation that will, hopefully, more accurately reflect the results captured experimentally.

REFERENCES

[1] G. I. I. Forum, "Generation iv systems," 2017.

[2] F. S. Sarikurt, *CFD Simulations of Erosion of a Stratified Layer by a Buoyant Jet in a Large Vessel*. PhD thesis, 2015.

[3] U. NRC, "The pressurized water reactor," *https://www.nrc.gov*, 2018.

[4] D. Krug, *Experimental investigation of the turbulent/non-turbulent interface in a gravity current*. PhD thesis, 2014.

[5] C. Vallée, D. Lucas, M. Beyer, H. Pietruske, H. Carl, *et al.*, "Experimental study on the air/water counter-current flow limitation in a model of the hot leg of a pressurized water reactor," *Nuclear Engineering and Design*, vol. 238, no. 12, pp. 3389–3402, 2008.

[6] D. D. LIANTO, T. HÖHNE, D. LUCAS, C. VALLEE, and G. A. MONTOYA ZABALA, "Cfd studies on the phenomena around counter-current flow limitations of gas," *Nuclear engineering and design*, vol. 241, no. 12, pp. 5138–5148, 2011.

[7] D. Lucas, M. Beyer, H. Pietruske, and L. Szalinski, "Counter-current flow limitation for air-water and steam-water flows in a pwr hot leg geometry," *Nuclear Engineering and Design*, vol. 323, pp. 56–67, 2017.

[8] S. Kliem, T. Sühnel, U. Rohde, T. Höhne, H.-M. Prasser, and F.-P. Weiss, "Experiments at the mixing test facility rocom for benchmarking of cfd codes," *Nuclear engineering and design*, vol. 238, no. 3, pp. 566–576, 2008.

[9] T. Toppila, "Cfd simulation of fortum pts experiment," *Nuclear Engineering and Design*, vol. 238, no. 3, pp. 514–521, 2008.

[10] T. Höhne, S. Kliem, and U. Bieder, "Modeling of a buoyancy-driven flow experiment at the rocom test facility using the cfd codes cfx-5 and trio_u," *Nuclear Engineering and Design*, vol. 236, no. 12, pp. 1309–1325, 2006.

[11] U. EIA, "Pressurized water reactor vessel," *http://www.eia.doe.gov*, 2018.

[12] A. Prošek, B. Končar, and M. Leskovar, "Uncertainty analysis of cfd benchmark case using optimal statistical estimator," *Nuclear Engineering and Design*, 2016.

[13] A. Shams, G. Damiani, D. Rosa, and E. Komen, "Design of a single-phase pts numerical experiment for a reference direct numerical simulation," *Nuclear Engineering and Design*, vol. 300, pp. 282–296, 2016.

[14] J. Kickhofel, H.-M. Prasser, P. K. Selvam, E. Laurien, and R. Kulenovic, "T-junction cross-flow mixing with thermally driven density stratification," *Nuclear Engineering and Design*, vol. 309, pp. 23–39, 2016.

[15] V. Petrov and A. Manera, "Effect of pump-induced cold-leg swirls on the flow field in the rpv of the eprâĎć: Cfd investigations and comparison with experimental results," *Nuclear Engineering and Design*, vol. 241, no. 5, pp. 1478–1485, 2011.

[16] W. Xu, Q. Chen, and F. Nieuwstadt, "A new turbulence model for near-wall natural convection," *International Journal of Heat and Mass Transfer*, vol. 41, no. 21, pp. 3161–3176, 1998.

[17] C. Gualtieri, A. Angeloudis, F. Bombardelli, S. Jha, and T. Stoesser, "On the values for the turbulent schmidt number in environmental flows," *Fluids*, vol. 2, no. 2, p. 17, 2017.

[18] Y. Tominaga and T. Stathopoulos, "Turbulent schmidt numbers for cfd analysis with various types of flowfield," *Atmospheric Environment*, vol. 41, no. 37, pp. 8091–8099, 2007.

[19] G. He, Y. Guo, and A. T. Hsu, "The effect of schmidt number on turbulent scalar mixing in a jet-in-crossflow," *International Journal of Heat and Mass Transfer*, vol. 42, no. 20, pp. 3727–3738, 1999.

[20] I. B. Celik, U. Ghia, P. J. Roache, *et al.*, "Procedure for estimation and reporting of uncertainty due to discretization in {CFD} applications," *Journal of fluids {Engineering-Transactions} of the {ASME}*, vol. 130, no. 7, 2008.

[21] . K. V. Orea, D., "Cold leg mixing cfd-uq benchmark open test," vol. 1, no. pp1-12, 2018.